The Astrophysical Journal, 964:183 (22pp), 2024 April 1 https://doi.org/10.3847/1538-4357/ad27cc
© 2024. The Author(s). Published by the American Astronomical Society.
OPEN ACCESS

Mapping the Growth of Supermassive Black Holes as a Function of Galaxy Stellar Mass and Redshift

Fan Zou[1,2], Zhibo Yu[1,2], W. N. Brandt[1,2,3], Hyungsuk Tak[1,4,5], Guang Yang[6,7], and Qingling Ni[8]
[1] Department of Astronomy and Astrophysics, 525 Davey Lab, The Pennsylvania State University, University Park, PA 16802, USA; fanzou01@gmail.com
[2] Institute for Gravitation and the Cosmos, The Pennsylvania State University, University Park, PA 16802, USA
[3] Department of Physics, 104 Davey Laboratory, The Pennsylvania State University, University Park, PA 16802, USA
[4] Department of Statistics, The Pennsylvania State University, University Park, PA 16802, USA
[5] Institute for Computational and Data Sciences, The Pennsylvania State University, University Park, PA 16802, USA
[6] Kapteyn Astronomical Institute, University of Groningen, P.O. Box 800, 9700 AV Groningen, The Netherlands
[7] SRON Netherlands Institute for Space Research, Postbus 800, 9700 AV Groningen, The Netherlands
[8] Max-Planck-Institut für extraterrestrische Physik (MPE), Gießenbachstraße 1, D-85748 Garching bei München, Germany
Received 2023 October 17; revised 2024 January 30; accepted 2024 February 7; published 2024 March 29

Abstract

The growth of supermassive black holes is strongly linked to their galaxies. It has been shown that the population mean black hole accretion rate ($\overline{\mathrm{BHAR}}$) primarily correlates with the galaxy stellar mass ($M_\star$) and redshift for the general galaxy population. This work aims to provide the best measurements of $\overline{\mathrm{BHAR}}$ as a function of $M_\star$ and redshift over ranges of $10^{9.5} < M_\star < 10^{12}\,M_\odot$ and $z < 4$. We compile an unprecedentedly large sample with 8000 active galactic nuclei (AGNs) and 1.3 million normal galaxies from nine high-quality survey fields following a wedding cake design. We further develop a semiparametric Bayesian method that can reasonably estimate $\overline{\mathrm{BHAR}}$ and the corresponding uncertainties, even for sparsely populated regions in the parameter space. $\overline{\mathrm{BHAR}}$ is constrained by X-ray surveys sampling the AGN accretion power and UV-to-infrared multiwavelength surveys sampling the galaxy population. Our results can independently predict the X-ray luminosity function (XLF) from the galaxy stellar mass function (SMF), and the prediction is consistent with the observed XLF. We also try adding external constraints from the observed SMF and XLF. We further measure $\overline{\mathrm{BHAR}}$ for star-forming and quiescent galaxies and show that star-forming $\overline{\mathrm{BHAR}}$ is generally larger than or at least comparable to the quiescent $\overline{\mathrm{BHAR}}$.

Unified Astronomy Thesaurus concepts: Supermassive black holes (1663); X-ray active galactic nuclei (2035); Galaxies (573)

1. Introduction

Supermassive black holes (SMBHs) and galaxies appear to be fundamentally linked (e.g., Kormendy & Ho 2013). Especially the SMBH mass (M_{BH}) and the galaxy bulge mass are found to be tightly correlated in the local universe, and the cosmic evolution of the SMBH accretion density and the star formation density are broadly similar and both peak at $z \approx 2$. Therefore, it is a fundamental question in extragalactic astronomy to understand how cosmic SMBH growth depends on galaxy properties.

SMBHs grow primarily through rapid accretion when they are observed as active galactic nuclei (AGNs); mergers are an additional growth mode. X-ray emission is known to be a good indicator of AGN activity because of its universality among AGNs, high penetrating power through obscuration, and low dilution from galaxy starlight (e.g., Brandt & Alexander 2015; Brandt & Yang 2022). Therefore, X-ray surveys can be used to constrain the accretion distribution and the black hole accretion rate ($\mathrm{BHAR} = dM_{\mathrm{BH}}/dt$) of SMBHs (e.g., Aird et al. 2012, 2018; Bongiorno et al. 2012, 2016; Georgakakis et al. 2017; Wang et al. 2017; Yang et al. 2017; Yang et al. 2018; Ni et al. 2019; Yang et al. 2019; Ni et al. 2021b). However, the duration of a galaxy within the AGN phase is relatively short, and AGNs also have strong variability (e.g., Hickox et al. 2014; Yang et al. 2016); thus, BHAR is often averaged over a large galaxy sample as an estimator of $\overline{\mathrm{BHAR}}$, the long-term population mean BHAR.

$\overline{\mathrm{BHAR}}$ has been shown to be redshift dependent and correlated with both stellar mass ($M_\star$) and star formation rate (SFR), while the $M_\star$ dependence is more fundamental for the general galaxy population (e.g., Hickox et al. 2014; Yang et al. 2017, 2018). In recent years, it has been found that $\overline{\mathrm{BHAR}}$ is also strongly related to galaxy morphology (e.g., Ni et al. 2019; Yang et al. 2019; Ni et al. 2021a; Aird et al. 2022), which may be more fundamental than the $\overline{\mathrm{BHAR}}$–$M_\star$ relation. However, such morphological measurements are expensive to obtain and require superb image resolution from, e.g., the Hubble Space Telescope, which inevitably are limited to small sky areas and thus can only provide a limited sample size covering a limited parameter space. In contrast, $M_\star$ and SFR are much more accessible. Notably, modern multiwavelength photometric surveys have provided extensive photometric data, based on which $M_\star$ and SFR can be estimated by fitting the corresponding spectral energy distributions (SEDs; e.g., Zou et al. 2022). Therefore, a well-measured $\overline{\mathrm{BHAR}}$–$M_\star$ relation is still essential to link SMBHs and galaxies.

The latest version of $\overline{\mathrm{BHAR}}$ as a function of ($M_\star$, z) was derived in Yang et al. (2018) using the data from the Cosmic Evolution Survey (COSMOS; Laigle et al. 2016; Weaver et al. 2022), Great Observatories Origins Deep Survey (GOODS)-S, and GOODS-N (Grogin et al. 2011; Koekemoer et al. 2011). Although the relation in Yang et al. (2018) has proved to be successful over the years, there are still some limitations. First, although COSMOS, GOODS-S, and GOODS-N are

Original content from this work may be used under the terms of the Creative Commons Attribution 4.0 licence. Any further distribution of this work must maintain attribution to the author(s) and the title of the work, journal citation and DOI.

sufficiently deep to probe $\overline{\mathrm{BHAR}}$ up to $z \approx 4$, they cannot effectively sample the last half of cosmic time ($z \lesssim 0.8$) because of their limited sky areas. Second, Yang et al. (2018) adopted strong assumptions when parametrically estimating $\overline{\mathrm{BHAR}}$, which may lead to underestimated $\overline{\mathrm{BHAR}}$ uncertainties. Built upon Yang et al. (2018), this work aims to provide the best available map of $\overline{\mathrm{BHAR}}(M_\star, z)$ with the currently best data and statistical methodology. Now is indeed the right time to remeasure $\overline{\mathrm{BHAR}}$ given the fact that the past 5 yr have witnessed the completion of several large, sensitive X-ray surveys in fields together with deep optical-to-IR surveys (e.g., Chen et al. 2018; Ni et al. 2021a). These new X-ray surveys, when combined with previous ones, can return a large AGN sample over 10 times larger than previous ones, as will be discussed in Section 2. In this work, we compile an unprecedentedly large sample from nine well-studied survey fields, many of which were finished after Yang et al. (2018) and even within $\lesssim$2 yr before this work. Our adopted surveys follow a wedding cake design and contain both deep, pencil-beam and shallow, wide ones, allowing us to effectively explore a wide range of parameter space. We further develop a semiparametric Bayesian approach that can return reasonable estimations and uncertainties, even for sparsely populated regions in the parameter space.

This work is structured as follows. Section 2 describes the data. Section 3 presents our methodology and $\overline{\mathrm{BHAR}}$ measurements. In Section 4, we discuss the implications of our results. Section 5 summarizes this work. We adopt a flat ΛCDM cosmology with $H_0 = 70\,\mathrm{km\,s^{-1}\,Mpc^{-1}}$, $\Omega_\Lambda = 0.7$, and $\Omega_M = 0.3$.

2. Data and Sample

We use the data within the Cosmic Assembly Near-Infrared Deep Extragalactic Legacy Survey (CANDELS) fields, four of the Vera C. Rubin Observatory Legacy Survey of Space and Time (LSST) Deep-Drilling Fields (DDFs), and eROSITA Final Equatorial Depth Survey (eFEDS) field. CANDELS and the LSST DDFs both contain several distinct fields, and we put those individual fields sharing similar areas and depths under the same umbrella (CANDELS or LSST DDFs) for convenience. Our adopted fields have X-ray coverage to provide AGN information and quality multiwavelength data, which are essential for measuring galaxy properties. We summarize our field information in Table 1 and discuss them in the following subsections.

2.1. CANDELS Fields

CANDELS (Grogin et al. 2011; Koekemoer et al. 2011) is a pencil-beam survey covering five fields—GOODS-S (0.05 deg^2), GOODS-N (0.05 deg^2), Extended Groth Strip (EGS; 0.06 deg^2), UKIRT Infrared Deep Sky Survey Ultra-Deep Survey (UDS; 0.06 deg^2), and a tiny part of COSMOS (denoted as CANDELS-COSMOS, hereafter; 0.06 deg^2). All the fields have ultra-deep UV-to-IR data (see, e.g., Yang et al. 2019 and references therein), allowing for detections of galaxies up to high redshift and low $M_\star$ and reliable measurements of these galaxies' properties. The first four have deep Chandra observations reaching ∼megasecond depths from (Luo et al. 2017; GOODS-S), (Xue et al. 2016; GOODS-N), (Nandra et al. 2015; EGS), and (Kocevski et al. 2018; UDS) and can thus effectively sample AGNs at high redshift and/or low luminosity. However, CANDELS-COSMOS shares the same X-ray depth as the full COSMOS field, and CANDELS-COSMOS is much smaller. Therefore, we do not use CANDELS-COSMOS but instead will directly analyze the full COSMOS field in Section 2.2.

We adopt the galaxy-property catalog in Yang et al. (2019), who measured $M_\star$ and SFRs by fitting SEDs for all the CANDELS sources.

2.2. LSST DDFs

The LSST DDFs (e.g., Brandt et al. 2018; Zou et al. 2022) include five fields—COSMOS, Wide Chandra Deep Field-South (W-CDF-S), European Large-Area Infrared Space Observatory Survey-S1 (ELAIS-S1), XMM-Newton Large Scale Structure (XMM-LSS), and Euclid Deep Field-South (EDF-S). EDF-S has been selected as an LSST DDF only recently in 2022 and currently does not have sufficient data available, and we thus only use the former four original LSST DDFs with superb data accumulated over approximately a decade. Note that this work does not use any actual LSST data because the Vera C. Rubin Observatory is still under construction at the time of writing this article.

COSMOS is a deg^2-scale field with deep multiwavelength data (e.g., Weaver et al. 2022). Civano et al. (2016) presented medium-depth (≈160 ks) Chandra observations in COSMOS. The galaxy properties measured through SED fitting covering the X-ray to far-IR are taken from Yu et al. (2023). We only use the region with "FLAG_COMBINED = 0" (i.e., within the UltraVISTA region and far from bright stars and image edges) in Weaver et al. (2022) to ensure quality multiwavelength characterizations. Ni et al. (2021a) presented ≈30 ks XMM-Newton observations in ELAIS-S1 and W-CDF-S, and Chen et al. (2018) presented ≈40 ks XMM-Newton observations in XMM-LSS. The galaxy properties in these three fields are taken from Zou et al. (2022). We limit our analyses to the overlapping region between the X-ray catalogs and Zou et al. (2022) because quality multiwavelength data are essential for estimating photometric redshifts (photo-zs), $M_\star$, and SFRs. Besides, GOODS-S and UDS in Section 2.1 are embedded within W-CDF-S and XMM-LSS, respectively, and we remove the regions covered by GOODS-S and UDS to avoid double counting sources. Due to these reasons, our areas are slightly smaller than those reported in Chen et al. (2018) and Ni et al. (2021a).

2.3. eFEDS

eFEDS is a 10^2 deg^2-scale field covered by eROSITA with ≈2 ks observations (Brunner et al. 2022). We focus on the 60 deg^2 GAMA09 region (Driver et al. 2022) within eFEDS because the remaining parts do not have sufficient multi-wavelength data to constrain the host-galaxy properties (e.g., Salvato et al. 2022). Unlike Chandra or XMM-Newton, eROSITA mostly works at <2.3 keV, which is more sensitive to obscuration. We thus rely on the X-ray properties cataloged in Liu et al. (2022) for eFEDS sources, which are measured through detailed X-ray spectral fitting and thereby can largely overcome obscuration effects. As suggested in Liu et al. (2022), we only use sources with detection likelihoods >10 because fainter sources generally do not allow meaningful X-ray spectral analyses.

Table 1
Basic Information on the Fields Used in This Work

Field	Area (deg^2)	m_{lim} (AB mag)	X-Ray Depth (ks)	X-Ray References	Galaxy References	Photo-z References	AGN	Galaxies	(a, b)
(1)	(2)	(3)	(4)	(5)	(6)	(7)	(8)	(9)	(10)
GOODS-S	0.05	26.5 (H)	7000 (Chandra)	5	1	4,8	224 (111)	4144	(−15.87, 2.63)
GOODS-N	0.05	26.5 (H)	2000 (Chandra)	8	1	1,11	174 (167)	4603	(−15.49, 2.58)
EGS	0.06	26.5 (H)	800 (Chandra)	6	1	9	112 (10)	5889	(−15.13, 3.08)
UDS	0.06	26.5 (H)	600 (Chandra)	4	1	8	117 (25)	5010	(−15.05, 4.90)
COSMOS	1.27	24 (K_s)	160 (Chandra)	3	2	5,10	1459 (880)	86765	(−14.68, 5.19)
ELAIS-S1	2.93	23.5 (K_s)	30 (XMM-Newton)	7	3	6,12	676 (261)	157791	(−13.90, 4.57)
W-CDF-S	4.23	23.5 (K_s)	30 (XMM-Newton)	7	3	6,12	872 (311)	210727	(−13.86, 4.97)
XMM-LSS	4.20	23.5 (K_s)	40 (XMM-Newton)	2	3	2	1765 (898)	254687	(−14.09, 5.36)
eFEDS	59.75	22 (Z)	2 (eROSITA)	1	2	3,7	2667 (1156)	615068	(−13.51, 2.59)

Notes. Column (1): field names. GOODS-S, GOODS-N, EGS, and UDS belong to CANDELS and are discussed in Section 2.1. COSMOS, ELAIS-S1, W-CDF-S, and XMM-LSS belong to the LSST DDFs and are discussed in Section 2.2. eFEDS is discussed in Section 2.3. Column (2): sky areas of the fields, only accounting for the regions we are using. Column (3): the limiting AB magnitudes we adopted in Section 2.4 to calculate the $M_\star$ completeness curves, and the reference bands are written within parentheses. Column (4): the typical depths in exposure time of the X-ray surveys, and the parentheses list the observatories with which our adopted X-ray surveys were conducted. For XMM-Newton, the reported exposure is the typical flare-filtered one for a single EPIC camera. All three EPIC cameras (one EPIC-pn and two EPIC-MOS) were used for the XMM-Newton observations, adding ≈80–100 ks EPIC exposure in total. The "a" parameter values in column (10) of this table represent typical flux limits in 2–10 keV. Column (5): the references for the X-ray surveys. Column (6): the references for our adopted host-galaxy properties. All of these references have appropriately considered the AGN emission for AGNs. Column (7): representative references examining the photo-zs in the corresponding fields. Column (8): number of AGNs. The parentheses list the numbers of sources with spec-zs. The surface number density of eFEDS AGNs is much smaller than those in the other fields primarily because the eFEDS limiting magnitude is much brighter. Column (9): number of normal galaxies. Column (10): the parameters describing the X-ray detection function; see Equation (3). There is a subtle difference between eFEDS and other fields—the eFEDS X-ray detection function is for the intrinsic 2–10 keV flux, while the others are for the observed flux.
X-ray references. (1) Brunner et al. (2022); (2) Chen et al. (2018); (3) Civano et al. (2016); (4) Kocevski et al. (2018); (5) Luo et al. (2017); (6) Nandra et al. (2015); (7) Ni et al. (2021a); (8) Xue et al. (2016).
Galaxy references. (1) Yang et al. (2019); (2) Yu et al. (2023); (3) Zou et al. (2022).
Photo-z references. (1) Barro et al. (2019); (2) Chen et al. (2018); (3) Driver et al. (2022); (4) Luo et al. (2017); (5) Marchesi et al. (2016); (6) Ni et al. (2021a); (7) Salvato et al. (2022); (8) Santini et al. (2015); (9) Stefanon et al. (2017); (10) Weaver et al. (2022); (11) Xue et al. (2016); (12) Zou et al. (2021).

2.4. Sample Construction

Sources in these fields all have either spectroscopic redshifts (spec-zs) or high-quality photo-zs, as have been extensively examined in previous literature. Representative examples are listed in column (7) of Table 1. Many more successful works built upon these redshifts have also indirectly justified their general reliability. When compared to the available spec-zs, the photo-zs are of high quality—our sample has a $\sigma_{\rm NMAD}$ of 0.03 (0.04) and an outlier fraction of 4% (15%) for galaxies (AGNs).[9] Spec-zs are adopted when available, and half of the involved AGNs have spec-zs.

We select sources with $0.05 < z < 4$ and $(\log M_{\star,\rm min} = 9.5) < \log M_\star < (\log M_{\star,\rm max} = 12)$. Sources labeled as stars are removed, as has been presented in the references in column (6) of Table 1. Only $\lesssim$15% of sources in each field are classified as stars. We apply a lower cut for z because photo-zs are less reliable when too small (e.g., see Appendix C of Zou et al. 2021), and the peculiar motions become nonnegligible as well. We limit $\log M_\star > 9.5$ because dwarf AGNs usually have much less reliable measurements and require special treatment (e.g., Zou et al. 2023). We apply the same upper cuts as in Yang et al. (2018) for both $M_\star$ and z because very few sources can exceed these thresholds.

We further construct a complete sample by applying redshift-dependent $M_\star$ cuts. To estimate the $M_\star$ depth for each field, we first adopt a reference band and denote its limiting magnitude as $m_{\rm lim}$. Following Pozzetti et al. (2010), we convert the magnitude depth to the expected limiting $M_\star$ for each galaxy with a magnitude of m: $\log M_{\rm lim} = \log M_\star + 0.4(m - m_{\rm lim})$. At each redshift, we adopt the $M_\star$ completeness threshold as the value above which 90% of the $M_{\rm lim}$ values lie. Sources below the $M_\star$ completeness curves are removed. For the CANDELS fields, we adopt the H band with a limiting magnitude of 26.5 mag, and almost all the sources above our $\log M_\star$ cut of 9.5 are above the CANDELS $M_\star$ completeness curves, enabling constraints upon $\overline{\rm BHAR}$ in the low-$M_\star$ and high-z regime. For the LSST DDFs, we adopt the K_s band, and their limiting K_s magnitudes are 24 for COSMOS (Laigle et al. 2016) and 23.5 for W-CDF-S, ELAIS-S1, and XMM-LSS (Jarvis et al. 2013), respectively. For eFEDS, we adopt the Z band with a limiting magnitude of 22. These $M_\star$ completeness cuts also automatically ensure the general SED-fitting reliability. The typical i-band magnitudes of sources at these limiting magnitudes are $i \approx 24.8$ at $K_s = 23.5$, $i \approx 25.3$ at $K_s = 24$, and $i \approx 22.4$ at $Z = 22$. These i-band magnitudes are roughly equal to the nominal *depths* of SEDs in (Zou et al. 2022; see their Figure 30) and Yu et al. (2023), below which the number of available photometric bands may become small.

We then define $\lambda = L_{\rm X}/M_\star$, where $L_{\rm X}$ is the intrinsic 2–10 keV luminosity, and we always adopt erg s^{-1} $M_\odot^{-1}$ as the unit for λ. We use the X-ray surveys mentioned in the previous subsections to select AGNs. Following Aird et al. (2012) and Yang et al. (2018), we only use sources detected in the hard band (HB)[10] for CANDELS and the LSST DDFs. The reason is to minimize the effects of obscuration. Selecting AGNs in soft bands (<2 keV) is biased toward little or no absorption. Since the obscuration level is known to be correlated with λ (e.g., Ricci et al. 2017), soft-band-selected AGNs are expected to be biased in terms of λ. Besides, our analyses need intrinsic $L_{\rm X}$, and HB fluxes are the least affected by obscuration. To calculate $L_{\rm X}$, and consequently, λ of these HB-detected sources, we use Equation A4 in Zou et al. (2022) and adopt a photon index of 1.6. As discussed in Yang et al. (2018), a photon index of 1.6 returns $L_{\rm X}$ agreeing the best with those from X-ray spectral fitting. For eFEDS, as mentioned in Section 2.3, we use the de-absorbed 0.5–2 keV flux in Liu et al. (2022) and convert it to $L_{\rm X}$ assuming a photon index of 1.8. Although eROSITA observations are more prone to obscuration effects, and it is less accurate to measure $L_{\rm X}$ with soft X-rays below ≈2 keV, we have verified in Appendix C that our median results remain similar when excluding eFEDS. It should be noted that we do not exclusively rely upon eFEDS to provide constraints at low-z and/or high-$M_\star$. The LSST DDFs, especially with the X-ray coverage in Chen et al. (2018) and Ni et al. (2021a) added, already have 12.6 deg^2 of coverage with useful HB sensitivity (see Table 1), and thus can also provide beneficial constraints. We define AGNs as those with $\log \lambda > \log \lambda_{\rm min} = 31.5$ and neglect the contribution of SMBHs with $\lambda \leqslant \lambda_{\rm min}$ to $\overline{\rm BHAR}$. This is because few of the X-ray-detected AGNs are below $\lambda_{\rm min}$, and the emission from X-ray binaries may become nonnegligible for low-λ sources. As we will show in Section 3.3, $\overline{\rm BHAR}$ is indeed dominated by sources above $\lambda_{\rm min}$.

In total, we have 8000 AGNs and 1.3 million normal galaxies, and they are plotted in the z–$M_\star$ and z–λ planes in Figure 1, where each column presents fields with comparable depths and areas. Note that Yang et al. (2019); Zou et al. (2022), and Yu et al. (2023), from which our adopted galaxy properties are taken, all have appropriately considered the AGN emission for AGNs. We will also assess the impact of AGNs that dominate the SEDs in Appendix D.

3. Method and Results

Denoting $p(\lambda|M_\star, z)$ as the conditional probability density per unit $\log \lambda$ of a galaxy with $(M_\star, z)$ hosting an AGN with λ and $k_{\rm bol}(L_{\rm X})$ as the $L_{\rm X}$-dependent 2–10 keV bolometric correction (i.e., the ratio between the AGN bolometric luminosity and $L_{\rm X}$), $\overline{\rm BHAR}$ can be expressed as follows:

$$\overline{\rm BHAR}(M_\star, z) = \int_{\log \lambda_{\rm min}}^{+\infty} \frac{(1-\epsilon) k_{\rm bol}(M_\star \lambda) M_\star \lambda}{\epsilon c^2} p(\lambda|M_\star, z) d\log\lambda, \quad (1)$$

where ϵ is the radiative efficiency of the accretion. The key step in measuring $\overline{\rm BHAR}$ is hence to derive $p(\lambda|M_\star, z)$. Some literature models the $L_{\rm X}$ distribution instead of λ (e.g., Aird et al. 2012). These two approaches are equivalent, and $p(\lambda|M_\star, z)$ and $p(L_{\rm X}|M_\star, z)$ are interchangeable. The only reason for choosing one instead of the other is for convenience, as λ is a scaled parameter that can serve as a rough proxy for the Eddington ratio.

[9] Defining $\Delta z = z_{\rm phot} - z_{\rm spec}$, $\sigma_{\rm NMAD}$ is then the normalized median absolute deviation of $\Delta z/(1 + z_{\rm spec})$, and outlier fraction is the fraction of sources with $|\Delta z|/(1 + z_{\rm spec}) > 0.15$. These two parameters are standard metrics used to represent the photo-z quality.

[10] The detection energy range for the HB has slightly different definitions in different fields—2–7 keV for CANDELS and COSMOS, 2–12 keV for W-CDF-S and ELAIS-S1, and 2–10 keV for XMM-LSS.

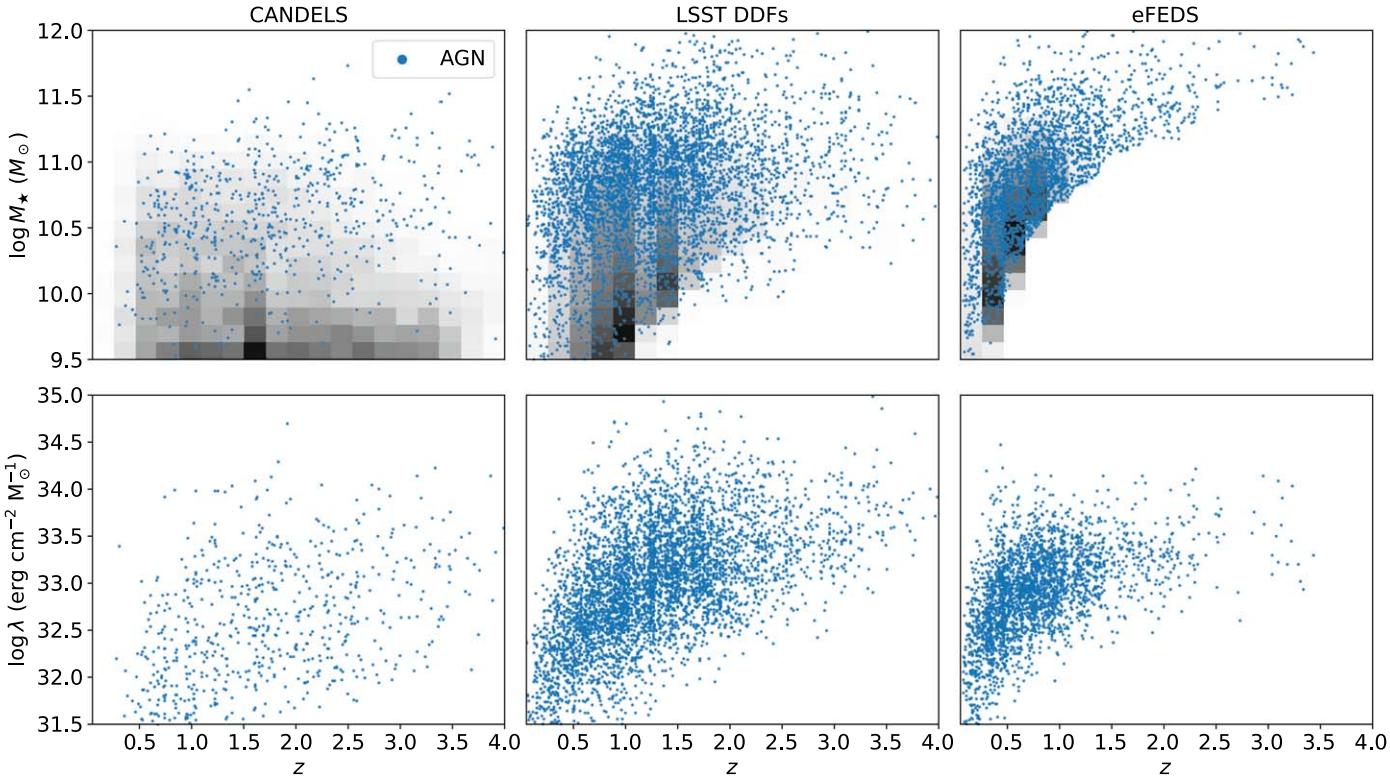

Figure 1. Our sample in the $z-M_\star$ (top) and $z-\lambda$ (bottom) planes. The left, middle, and right panels are for CANDELS, the LSST DDFs, and eFEDS, respectively. The points are AGNs. The background grayscale cells in the left panel are the 2-D histogram of the number of normal galaxies, with darker cells representing more galaxies. The apparent deficiency of sources in the high-z and/or low-$M_\star$ regime in the middle and right panels is due to our $M_\star$ completeness cuts.

3.1. Semiparametric Modeling of p(λ|M$_\star$, z)

We assume a double power law with respect to λ for $p(\lambda|M_\star, z)$:

$$p(\lambda|M_\star, z) = \begin{cases} A\left(\frac{\lambda}{\lambda_c}\right)^{-\gamma_1}, & \lambda_{\rm min} < \lambda \leqslant \lambda_c \\ A\left(\frac{\lambda}{\lambda_c}\right)^{-\gamma_2}, & \lambda > \lambda_c \end{cases}. \quad (2)$$

The four parameters (A, λ_c, γ_1, γ_2) are functions of ($M_\star$, z). We require $\lambda_c > \lambda_{\rm min}$ because, otherwise, the model will always degenerate to a single power law and has no dependence on γ_1 once λ_c lies below $\lambda_{\rm min}$. We also require $\gamma_2 > 0$; otherwise, $p(\lambda|M_\star, z)$ will not be a probability measure, and the model-predicted number of AGNs will diverge.[11] It has been shown that a double power law can indeed approximate $p(\lambda|M_\star, z)$ well (e.g., Bongiorno et al. 2016; Aird et al. 2018; Yang et al. 2018). Similarly, the observed AGN X-ray luminosity function (XLF) also follows a double power law (e.g., Ueda et al. 2014), and a $p(\lambda|M_\star, z)$ roughly with a double power-law shape is needed to reproduce the XLF (Section 3.2).

3.1.1. The Detection Probability

We denote $P_{\rm det}(f_{\rm X})$ as the probability that a source with a 2–10 keV flux of $f_{\rm X}$ is detected by a given X-ray survey. Following Section 3.4 in Zou et al. (2023), we adopt the following functional form for $P_{\rm det}(f_{\rm X})$:

$$P_{\rm det}(f_{\rm X}) = \frac{1}{2}[{\rm erf}(b(\log f_{\rm X} - a)) + 1], \quad (3)$$

where a and b are parameters determining the shape of $P_{\rm det}(f_{\rm X})$. We follow the same procedures as in Zou et al. (2023) to calibrate a and b and report the results in Table 1. Briefly, we compared the $f_{\rm X}$ distribution with the 2–10 keV $\log N - \log S$ relation in Georgakakis et al. (2008), which is the well-determined expected surface number density per unit $f_{\rm X}$ with the detection procedures deconvolved. The comparison can return best-fit (a, b) parameters such that the convolution between the $\log N - \log S$ relation and $P_{\rm det}$ best matches the observed $f_{\rm X}$ distribution. It is necessary to adopt a functional form because it improves the computational speed by several orders of magnitude, as will be discussed below. The form of Equation (3) has been shown to be appropriate for X-ray surveys (e.g., Yan et al. 2023; Zou et al. 2023) because its overall shape is similar to X-ray sensitivity curves, and in our case, it indeed returns consistent $\overline{\rm BHAR}$ as in Yang et al. (2018), who did not adopt this functional form for $P_{\rm det}$.

There is a subtle difference between eFEDS and the other fields. For the latter, their $f_{\rm X}$ is the observed value taken from the original X-ray catalogs. The $\log N - \log S$ relation is also for the observed $f_{\rm X}$; thus, $P_{\rm det}$ is for the observed $f_{\rm X}$. For eFEDS, we adopt the intrinsic, de-absorbed 0.5–2 keV flux in Liu et al. (2022) and multiply it by 1.57 to convert it to the *intrinsic* 2–10 keV flux assuming a photon index of $\Gamma = 1.8$. For consistency, we should correct the $\log N - \log S$ relation such that it works for the intrinsic $f_{\rm X}$. We use the XLF (ϕ_L) in Ueda

[11] Note that $p(\lambda|M_\star, z)$ is defined in the $\log\lambda$ space, and thus $\gamma_2 > 0$ is sufficient and necessary for $\int_{\log\lambda_{\rm min}}^{+\infty} p(\lambda|M_\star, z) d\log\lambda < +\infty$.

et al. (2014) to derive the correction. The XLF-predicted intrinsic $\log N - \log S$ relation is

$$N(f_{\rm X,int} > S) = A_{\rm all\ sky}^{-1} \int_{\log S}^{+\infty} \int_0^5 \phi_L(L_{\rm X}, z) \times \frac{dV_C}{dz} d\log f_{\rm X,int}\, dz, \quad (4)$$

$$L_{\rm X}(f_{\rm X,int}, z) = \frac{f_{\rm X,int}}{\eta(z)}, \quad (5)$$

$$\eta(z) = \frac{(1+z)^{2-\Gamma}}{4\pi D_L^2}, \quad (6)$$

where $A_{\rm all\ sky}$ is the all-sky solid angle, V_C is the comoving volume within a redshift of z, $\eta(z)$ is a function of z converting $L_{\rm X}$ to the intrinsic 2–10 keV flux for a power-law X-ray spectrum with a power-law photon index of $\Gamma = 1.8$, and D_L is the luminosity distance. We limit the integration to $z < 5$ because the contribution of higher-redshift sources to the total source number is negligible. Similarly, the predicted observed $\log N - \log S$ relation is

$$N(f_{\rm X,obs} > S) = A_{\rm all\ sky}^{-1} \int_{\log S}^{+\infty} \int_0^5 \int_{20}^{24} \phi_L(L_{\rm X}, z) \frac{dV_C}{dz} \times p(N_{\rm H}|L_{\rm X}, z) d\log f_{\rm X,obs}\, dz d\log N_{\rm H}, \quad (7)$$

$$L_{\rm X}(f_{\rm X,obs}, z, N_{\rm H}) = \frac{f_{\rm X,obs}}{\eta(z)\alpha(N_{\rm H}, z)}, \quad (8)$$

where the $N_{\rm H}$ function $p(N_{\rm H}|L_{\rm X}, z)$ is the conditional probability density per unit $\log N_{\rm H}$ of an AGN with ($L_{\rm X}$, z), as given in Section 3 of Ueda et al. (2014). This function is normalized such that $\int_{20}^{24} p(N_{\rm H}|L_{\rm X}, z) d\log N_{\rm H} = 1$. $\alpha(N_{\rm H}, z)$ is the absorption factor for a source with $\Gamma = 1.8$ and is calculated based on photoelectric absorption and Compton-scattering losses (i.e., `zphabs×cabs`) in `XSPEC`.

The XLF-predicted $N(f_{\rm X,obs} > S)$ is similar to the observed $\log N - \log S$ relation, with an absolute difference generally below 0.2 dex. We found that $\log[N(f_{\rm X,int} > S)/N(f_{\rm X,obs} > S)]$ is almost a constant around 0.15 dex at $\log S > 10^{-14}$ erg cm^{-2} s^{-1}, and thus we add 0.15 dex to the observed $\log N - \log S$ relation in Georgakakis et al. (2008) to approximate the intrinsic relation. Applying this intrinsic relation for our calibration in Equation (3), we can obtain the eFEDS $P_{\rm det}$ as a function of the intrinsic $f_{\rm X}$. Given that the intrinsic $f_{\rm X}$ instead of the observed $f_{\rm X}$ is always adopted in our analyses of eFEDS, the fact that eFEDS is more easily affected by absorption has been appropriately accounted for and absorbed into $P_{\rm det}$. For example, the fact that obscured AGNs may be missed by eFEDS causes the a value to slightly shift to a larger value due to the correction applied to the observed $\log N - \log S$ relation. One may wonder why we convert the 0.5–2 keV flux to 2–10 keV flux instead of directly using 0.5–2 keV flux. Since the intrinsic flux is always adopted, the conversion, in principle, would not cause systematic biases. The main reason is that the correction to the $\log N - \log S$ relation is considerably smaller for the 2–10 keV band than for the 0.5–2 keV band.

One caveat is that we limit the integration range of $N_{\rm H}$ in Equation (7) to be below 10^{24} cm^{-2}, which equivalently means that we neglect the contribution from Compton-thick (CT) AGNs with $N_{\rm H} > 10^{24}$ cm^{-2} for eFEDS. Similarly, in our other fields observed by Chandra or XMM-Newton, we also implicitly neglect most CT AGNs because they can hardly be detected even in the HB. Generally, X-ray observations below 10 keV cannot provide effective constraints for the CT population, and the intrinsic fraction of CT AGNs is highly uncertain (e.g., Ananna et al. 2019). Therefore, any attempt to measure the intrinsic CT population properties using X-rays below 10 keV is likely prone to large systematic uncertainties. The CT population might indeed contribute to the SMBH growth and is missed by our measurements, especially at high redshift (e.g., Yang et al. 2021), but observations in the regime insensitive to the CT obscuration are necessary to reveal it (e.g., Yang et al. 2023).

3.1.2. The Likelihood

When compared with the observed data, the log-likelihood function (e.g., Loredo 2004) is

$$\ln \mathcal{L} = -\sum_{s=1}^{n^{\rm gal}} T_{{\rm gal},s} + \sum_{s=1}^{n^{\rm AGN}} \ln p(\lambda_s|M_{\star,s}, z_s), \quad (9)$$

$$T_{\rm gal} = \int_{\log \lambda_{\rm min}}^{+\infty} p(\lambda|M_\star, z) P_{\rm det}(f_{\rm X}(\lambda M_\star, z)) d\log \lambda, \quad (10)$$

$$f_{\rm X}(\lambda M_\star, z) = \lambda M_\star \eta(z), \quad (11)$$

where $\eta(z)$ is given in Equation (6). We adopt $\Gamma = 1.8$ and 1.6 for eFEDS and the other fields, respectively. Different Γ values are adopted because the adopted $f_{\rm X}$ inside our $P_{\rm det}$ function is the intrinsic value for eFEDS, while being the observed one for the other fields (Section 3.1.1). Equation (10) involves an integration, and Equation (9) computes Equation (10) many times in the summation for a single evaluation of $\mathcal{L}$. Numerically integrating Equation (10) is slow, making it impractical to sample more than one or two dozen free parameters (as will be shown later, we will have 10^4 free parameters). Fortunately, as previously suggested in Zou et al. (2023), Equation (10) can be analytically solved when choosing appropriate functional forms for $p(\lambda|M_\star, z)$ and $P_{\rm det}(f_{\rm X})$, and our Equations (2) and (3) enable this. This is one of the most important steps enabling our whole semiparametric analyses.

We define

$$I(\gamma, \lambda_1, \lambda_2, A, \lambda_c; M_\star, z) = \int_{\log \lambda_1}^{\log \lambda_2} A\left(\frac{\lambda}{\lambda_c}\right)^{-\gamma} P_{\rm det}(\lambda M_\star \eta(z)) d\log \lambda. \quad (12)$$

Using Equation (21) in Zou et al. (2023), Equation (12) can be reduced as follows:

$$I = \frac{A}{2\gamma \ln 10}\left\{\left(\frac{\lambda_1}{\lambda_c}\right)^{-\gamma}[{\rm erf}(x_1)+1] - \left(\frac{\lambda_2}{\lambda_c}\right)^{-\gamma}[{\rm erf}(x_2)+1] - \left(\frac{10^{a-\frac{\gamma \ln 10}{4b^2}}}{\lambda_c M_\star \eta}\right)^{-\gamma}\left[{\rm erf}\left(x_1 + \frac{\gamma \ln 10}{2b}\right) - {\rm erf}\left(x_2 + \frac{\gamma \ln 10}{2b}\right)\right]\right\}, \quad (13)$$

$$x_k = b[\log(\lambda_k M_\star \eta) - a],\ k = 1, 2. \quad (14)$$

Equation (10) can then be expressed as follows:

$$T_{\rm gal}(A,\ \lambda_c,\ \gamma_1,\ \gamma_2;\ M_\star,\ z) = I(\gamma_1,\ \lambda_{\rm min},\ \lambda_c,\ A,\ \lambda_c;\ M_\star,\ z) + I(\gamma_2,\ \lambda_c,\ +\infty,\ A,\ \lambda_c;\ M_\star,\ z). \quad (15)$$

The above equations express $\mathcal{L}$ as a function of (A, λ_c, γ_1, γ_2), which themselves are functions of ($M_\star$, z). The dependences of (A, λ_c, γ_1, γ_2) on ($M_\star$, z) lack clear guidelines, and we use a nonparametric approach to model them. We divide the ($M_\star$, z) plane into $N_M \times N_z$ grids and adopt the (A, λ_c, γ_1, γ_2) values in each grid element as free parameters, i.e., we have $4N_MN_z$ free parameters in total. Such an approach is conceptually similar to and was indeed initially inspired by the *gold standard* nonparametric star formation history (e.g., Leja et al. 2019) in SED fitting. In a strict statistical sense, a method is called *nonparametric* only if the number of free parameters scales with the number of data points. In contrast, we used a fixed number of free parameters, which does not exactly satisfy the statistical definition. Although we can easily adjust N_M and N_z so that the number of free parameters scales with the number of data points, this makes the computation infeasible because we have millions of galaxies; besides, with our continuity prior in Section 3.1.3, further increasing the number of free parameters does not improve our results materially. In our context, we use the word nonparametric because our number of free parameters is far larger than that of typical parametric methods, and our method is effectively similar to the fully nonparametric approach. This same argument also works for *nonparametric star formation history* in, e.g., Leja et al. (2019).

This method has an important advantage over a parametric one in our case. As Figure 1 shows, most of our data are clustered within a small region of the ($M_\star$, z) plane—the number of sources significantly decreases at both low z ($\lesssim$0.8) and high z ($\gtrsim$2), the number of galaxies strongly depends on $M_\star$, and most AGNs are confined within $10^{10.5} \lesssim M_\star \lesssim 10^{11.2}\,M_\odot$. This indicates that if we assume any parametric form for (A, λ_c, γ_1, γ_2), the fitted parameters will be dominated by the small but well-populated region in the ($M_\star$, z) plane. Especially, one strong argument disfavoring parametric fitting is that our ultimate goal is to derive $\overline{\rm BHAR}$ across all redshifts, but any parametric fitting will return results dominated by sources in a small redshift range (e.g., Yang et al. 2018). Our semiparametric settings avoid this problem.

Equation (9) then becomes

$$\ln\mathcal{L} = \sum_{i=1}^{N_M}\sum_{j=1}^{N_z}[-n_{ij}^{\rm gal}T_{\rm gal}(A_{ij},\ \lambda_{c,ij},\ \gamma_{1,ij},\ \gamma_{2,ij};\ M_{\star,i},\ z_j) + \sum_{s=1}^{n_{ij}^{\rm AGN}}\ln p_{ij}(\lambda_s|M_{\star,s},\ z_s)], \quad (16)$$

where $n_{ij}^{\rm gal}$ and $n_{ij}^{\rm AGN}$ are the numbers of galaxies and AGNs within the (i, j) bin, respectively. $\mathcal{L}$ is defined for each individual survey field, and they are added together to return the final likelihood.

3.1.3. The Prior

We adopt a continuity prior of

$$X_{i+1,j} - X_{ij} \sim N\left(0,\ \frac{\sigma_X^2}{N_M}\right), \quad (17)$$

$$X_{i,j+1} - X_{ij} \sim N\left(0,\ \frac{\sigma_X^2}{N_z}\right), \quad (18)$$

where X denotes each one of ($\log A$, $\log\lambda_c$, γ_1, γ_2), and σ_X is our chosen a priori parameters to quantify the overall variations of X across the whole fitting ranges. The goal of this continuity prior is to transport information among grid elements. Without this prior, the fitted parameters in each grid element become unstable and vary strongly. This prior is defined in a way such that the information flow is roughly independent of the grid size. The continuity prior is defined only for the differences, and we need a further prior for the X's in a single cell and adopt it as flat in the ($\log A$, $\log\lambda_c$, γ_1, γ_2) space. We set bounds for these parameters to ensure propriety of the prior (Tak et al. 2018): $-10 < \log A < 10$, $\log\lambda_{\rm min} < \log\lambda_c < 40$, $-5 < \gamma_1 < 10$, and $0 < \gamma_2 < 10$. These ranges are sufficiently large to encompass any reasonable parameter values. Our posterior (Section 3.1.4) may also become less numerically stable outside these bounds. The resulting prior is explicitly shown below.

$$\ln\pi_{\rm cont} = -\frac{1}{2}\sum_X\left[N_M\sum_{i=1}^{N_M-1}\sum_{j=1}^{N_z}\frac{(X_{i+1,j}-X_{ij})^2}{\sigma_X^2} + N_z\sum_{i=1}^{N_M}\sum_{j=1}^{N_z-1}\frac{(X_{i,j+1}-X_{ij})^2}{\sigma_X^2}\right]. \quad (19)$$

Note that it is defined in the ($\log A$, $\log\lambda_c$, γ_1, γ_2) space, and an appropriate Jacobian determinant should be added when transforming the parameter space. For sampling purposes, variable transformations are usually needed.

We rely on previous literature to set appropriate values for σ_X. Yang et al. (2018) used a double power law similar to ours to fit $p(\lambda|M_\star,\ z)$, and their best-fit parameters (see their Equation (16)) span ranges of $-3.53 < \log A < -0.86$, $31.73 < \log\lambda_c < 34.98$, $\gamma_1 = 0.43$, and $1.55 < \gamma_2 < 3.55$ across our parameter spaces. Bongiorno et al. (2016) modeled the bivariate distribution function of $M_\star$ and λ for AGNs, which can be converted to $p(\lambda|M_\star,\ z)$ by dividing it by the galaxy stellar mass function (SMF), and the corresponding $p(\lambda|M_\star,\ z)$ is also a double power law. We use the SMF in Wright et al. (2018) for the conversion, and the best-fit double power-law parameters in Bongiorno et al. (2016) span ranges of $-5.28 < \log A < -0.08$, $33.32 < \log\lambda_c < 34.52$, $-0.67 < \gamma_1 < 1.62$, and $\gamma_2 = 3.72$. Aird et al. (2018) nonparametrically modeled $p(\lambda|M_\star,\ z)$, and we use our double power-law model to fit their results above $M_\star = 10^{9.5}\,M_\odot$ by minimizing the Kullback–Leibler divergence of our model relative to theirs. The returned best-fit values range between $-2.87 < \log A < -0.69$, $31.84 < \log\lambda_c < 34.04$, $-0.58 < \gamma_1 < 0.52$, and $0.72 < \gamma_2 < 1.67$. Another independent way to estimate $p(\lambda|M_\star,\ z)$ is based on the fact that $p(\lambda|M_\star,\ z)$, by definition, can predict the XLF when combined with the SMF (see Equation (22) and Section 4.1 for more details). We estimate

parameters of $p(\lambda|M_\star, z)$ such that when using the SMF in Wright et al. (2018), the predicted XLF can match the best with the XLF in Ueda et al. (2014). This returns $-2.81 < \log A < -1.08$, $32.72 < \log \lambda_c < 33.77$, $-0.35 < \gamma_1 < 0.90$, and $2.46 < \gamma_2 < 2.82$. Taking the union of these estimations, the ranges should span no more than $-5.28 < \log A < -0.08$, $31.73 < \log \lambda_c < 34.98$, $-0.67 < \gamma_1 < 1.62$, and $0.72 < \gamma_2 < 3.72$. We adopt σ_X as one-third of the widths,[12] i.e., $\sigma_{\log A} = 1.7$, $\sigma_{\log \lambda_c} = 1.1$, $\sigma_{\gamma_1} = 0.8$, and $\sigma_{\gamma_2} = 1.0$.

In fact, our prior setting is essentially a rasterized approximation to the continuous surface of a Gaussian process (GP) regression (e.g., Rasmussen & Williams 2006). This is because the blocky prior surface over the $(M_\star, z)$ plane becomes the nonparametric GP-based continuous surface as the resolution of the grid increases (i.e., increasing N_M and N_z to infinity). Therefore, a full GP regression involves a large number of free parameters scaling with the galaxy sample size ($\approx 10^6$), while our rasterized approach only involves 10^4 parameters. GP also requires computations of $\mathcal{O}(n^3)$ for matrix inversions, while our approach turns the matrix-inversion problem into products of multiple univariate Gaussian densities. Due to these reasons, a full GP regression is computationally infeasible in our case, but our approach effectively works similarly and is much less computationally demanding.

3.1.4. The Posterior

The posterior is

$$\ln \mathcal{P} = \sum_{\text{field}} \ln \mathcal{L} + \ln \pi_{\text{cont}}. \tag{20}$$

We call our overall modeling *semiparametric* because we adopt $p(\lambda|M_\star, z)$ as a parametric function of λ, while the dependences of $(A, \lambda_c, \gamma_1, \gamma_2)$ on $(M_\star, z)$ are nonparametric. Readers may wonder why we do not also adopt a nonparametric function for $p(\lambda|M_\star, z)$. In principle, it could be done and was presented in Georgakakis et al. (2017) and Aird et al. (2018). Since any model contains subjective assumptions, the choice of the methodology should be guided by the assumptions we want to retain or avoid. Compared to nonparametric modeling, the assumptions of parametric models are much stronger. We nonparametrically model $(A, \lambda_c, \gamma_1, \gamma_2)$ as functions of $(M_\star, z)$ because we genuinely do not know their dependencies and thus want to minimize assumptions. However, we are satisfied with and thus want to retain the inherent assumption of our parameterization of $p(\lambda|M_\star, z)$ that the true dependence is indeed well approximated by a double power law when $\lambda > \lambda_{\min}$. Previous works have shown that a double power law indeed works, and as far as we know, there is no clear evidence suggesting that this assumption would fail. Especially, the nonparametric form of $p(\lambda|M_\star, z)$ inferred from Aird et al. (2018) is also roughly a double power law. The adopted approach essentially depends on our ultimate goal. It is certainly better to minimize the assumption for $p(\lambda|M_\star, z)$ and adopt a nonparametric form for it if the ultimate goal is to derive the shape of $p(\lambda|M_\star, z)$. However, our goal is different—we are ultimately interested in $\overline{\text{BHAR}}$ and thus want to assume a double power-law form for $p(\lambda|M_\star, z)$.

[12] A nominal σ is often approximated by one-quarter of the range, according to the so-called *range rule of thumb*. We have two dimensions in our case, and thus the one dimension σ can be chosen as $1/(4\sqrt{2})$ of the range. However, we would like to be slightly more conservative. The reason is that previous works mostly do not cover a parameter space as large as this work, and thus extrapolations are employed when computing the ranges. Some conservativeness can enable more flexibility to accommodate possible systematic extrapolation errors in regimes not well covered by previous works.

3.2. Hamiltonian Monte Carlo Sampling of $p(\lambda|M_\star, z)$

Given the high dimensionality, Hamiltonian Monte Carlo (HMC; e.g., Betancourt 2017) should be one of the most practical methods to sample the posterior. As far as we know, other sampling methods either cannot work efficiently in our high-dimension case (e.g., the traditional Metropolis–Hastings algorithm) or do not have well-developed packages readily available (e.g., Bayer et al. 2023). HMC needs both the posterior and its gradient in the parameter space. The posterior has been presented in the previous subsections, and we present the gradient in Appendix A. We use `DynamicHMC.jl`[13] to conduct the HMC sampling. We adopt $N_M = 49$ and $N_z = 50$. The sampling results are presented in Figure 2. These parameter maps will be released online.

To examine our fitting quality, we compare the model $p(\lambda|M_\star, z)$ with the observed values. We use the $n_{\text{obs}}/n_{\text{mdl}}$ method to obtain binned estimators of $p(\lambda|M_\star, z)$, as outlined in Aird et al. (2012). For a given $(z, M_\star, \lambda)$ bin ranging from $[z_{\text{low}}, z_{\text{high}}] \times [M_{\star,\text{low}}, M_{\star,\text{high}}] \times [\lambda_{\text{low}}, \lambda_{\text{high}}]$, we denote the number of observed AGNs as n_{obs} and calculate the model-predicted number as n_{mdl}:

$$n_{\text{mdl}} = \sum_s \int_{\log \lambda_{\text{low}}}^{\log \lambda_{\text{high}}} p(\lambda|M_{\star,s}, z_s) P_{\text{det}}(f_{\text{X}}(\lambda M_{\star,s}, z_s)) d \log \lambda, \tag{21}$$

where the summation runs over all the sources within $[z_{\text{low}}, z_{\text{high}}] \times [M_{\star,\text{low}}, M_{\star,\text{high}}]$. The observed binned estimator of $p(\lambda|M_\star, z)$ is then the fitted model evaluated at the bin center scaled by $n_{\text{obs}}/n_{\text{mdl}}$, and its uncertainty is calculated from the Poisson error of n_{obs} following Gehrels (1986). We present our model $p(\lambda|M_\star, z)$ and the binned estimators in Figure 3, and they are consistent. The uncertainties become large especially in the high-z/low-$M_\star$ and low-z/high-$M_\star$ regimes because of a limited number of AGNs being available. In the high-z/low-$M_\star$ regime, most of the constraints are from deep CANDELS fields, especially GOODS-S, because the other fields are not sufficiently deep in both X-rays and other multiwavelength bands. For example, 60% (80%) of AGNs in our sample with $M_\star < 10^{10}\, M_\odot$ and $z > 2$ ($z > 3$) are from GOODS-S. At $z < 0.5$, $\gtrsim$60% of AGNs are from eFEDS, and even the 60 deg^2 eFEDS is not sufficiently large to effectively sample high-$M_\star$ sources at low redshift. We also plot several $p(\lambda|M_\star, z)$ results from previous works and leave more detailed discussions on the comparison between our $p(\lambda|M_\star, z)$ and previous ones in Section 4.2.

As another independent check, $p(\lambda|M_\star, z)$, by definition, can connect the SMF (ϕ_M) and XLF (ϕ_L). That is, the SMF and $p(\lambda|M_\star, z)$ can jointly predict the XLF (e.g., Bongiorno et al.

[13] https://www.tamaspapp.eu/DynamicHMC.jl/stable/

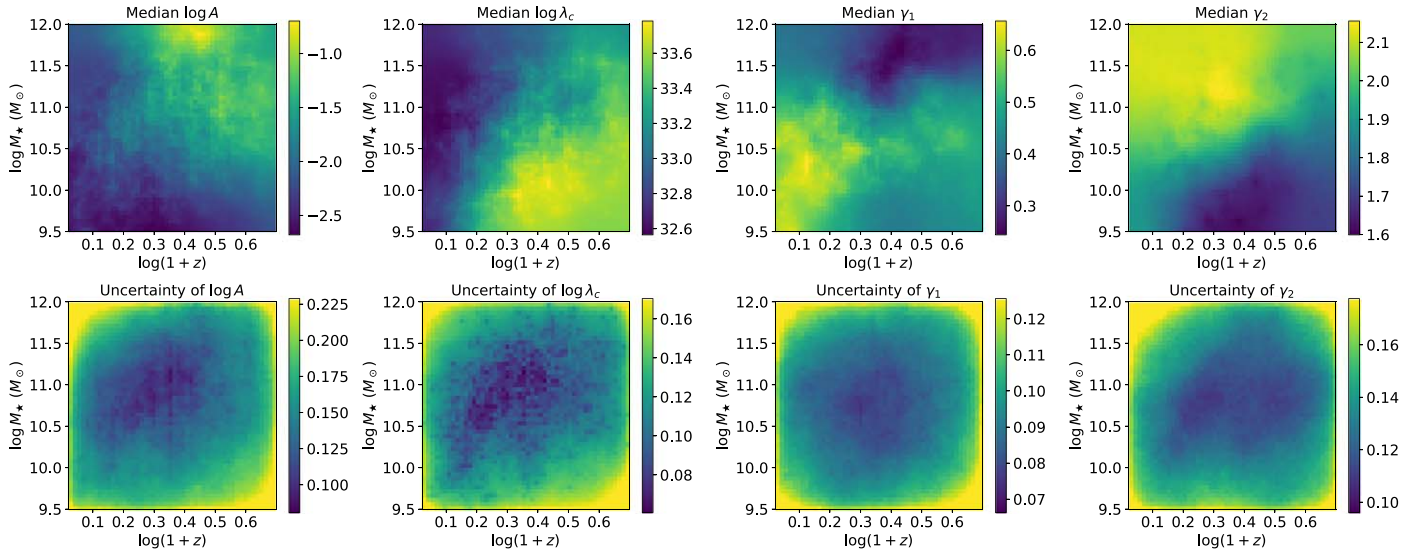

Figure 2. The sampled maps of (A, λ_c, γ_1, γ_2). The top panels are the median posteriors, and the bottom panels are the 1σ uncertainties, defined as the half-width of the posterior's 16th–84th percentile range.

2016; Georgakakis et al. 2017):

$$\phi_{L,\mathrm{mdl}}(L_\mathrm{X}, z) = \int_{\log M_{\star,\min}}^{\log M_{\star,\max}} p(\lambda|M_\star, z)\phi_M d\log M_\star = \int_{\log M_{\star,\min}}^{\log M_{\star,\max}} p(L_\mathrm{X}/M_\star|M_\star, z)\phi_M d\log M_\star. \quad (22)$$

Comparing $\phi_{L,\mathrm{mdl}}$ and the observed XLF, $\phi_{L,\mathrm{obs}}$, can thus further assess our fitting quality. We adopt ϕ_M in Wright et al. (2018) and the median parameter maps in Figure 2 to calculate $\phi_{L,\mathrm{mdl}}$. We present the comparison between $\phi_{L,\mathrm{mdl}}$ and $\phi_{L,\mathrm{obs}}$ from Ueda et al. (2014) in Figure 4, and they agree well. Note that for comparison purposes here, we do not need to optimize the computation of Equation (22); however, we will present a more optimized computation algorithm later in Section 4.1, where we do need fast computational speed. Also, note that Equation (22) ignores the contribution from sources with $M_\star$ below $M_{\star,\min} = 10^{9.5}\,M_\odot$ or above $M_{\star,\max} = 10^{12}\,M_\odot$ to the XLF. This is appropriate because the XLF is dominated by AGNs with $10^{9.5} < M_\star < 10^{12}\,M_\odot$. As a simple check, for the parameters in Figure 2, if we extrapolate the integration in Equation (22) to $(-\infty, +\infty)$, the typical $\phi_{L,\mathrm{mdl}}$ will only increase by 0.01 dex at $43 < L_\mathrm{X} < 43.5$, the lowest L_X bin that we will later adopt in Section 4.1. This increment is even smaller for higher L_X bins.

3.3. Measuring $\overline{\mathrm{BHAR}}$

Equation (1) converts $p(\lambda|M_\star, z)$ to $\overline{\mathrm{BHAR}}$. We adopt $\epsilon = 0.1$ and k_bol from Equation (2) in Duras et al. (2020). In principle, ϵ may depend upon other factors such as the accretion state (e.g., Yuan & Narayan 2014), but it is infeasible to accurately measure ϵ for our individual sources. We adopt ϵ as 0.1 because it is a typical value for the general AGN population (e.g., Brandt & Alexander 2015) and has been widely used in previous literature (e.g., Yang et al. 2017, 2018; Ni et al. 2019; Yang et al. 2019; Ni et al. 2021b). The k_bol relation in Duras et al. (2020) diverges at high L_X. To avoid it, we cap k_bol not to exceed 363, the value when the bolometric luminosity is $10^{14.5}\,L_\odot$, which is roughly the brightest sample used in Duras et al. (2020) to calibrate the k_bol relation. We show the L_X–k_bol relation in Figure 5, in which we also plot the relation used in Yang et al. (2018), derived from Lusso et al. (2012), for a comparison. The two relations are similar, with a small offset of ≈0.07 dex that is almost negligible compared to the $\overline{\mathrm{BHAR}}$ uncertainty (Figure 6). The deviation of the two relations at $L_\mathrm{X} \gtrsim 10^{45}\,\mathrm{erg\,s^{-1}}$ has little impact on $\overline{\mathrm{BHAR}}$ because $\overline{\mathrm{BHAR}}$ has little contribution from $\log\lambda \gtrsim 35$ (see Figure 3).

Equation (1) ignores the contribution to $\overline{\mathrm{BHAR}}$ from sources at $\log\lambda < 31.5$ because X-ray binaries may not be negligible at lower λ, and our X-ray surveys can hardly provide strong constraints in the low-λ regime. However, this will not cause material biases because $\overline{\mathrm{BHAR}}$ is dominated by sources at $\log\lambda \gtrsim 31.5$ (e.g., Section 3.2.3 in Yang et al. 2018). We have also tried pushing the lower integration bound in Equation (1) down by 2 dex, and the returned $\overline{\mathrm{BHAR}}$ would only increase by a typical value of ≈0.02 dex and no more than ≈0.1 dex. Such a difference is much smaller than the fitted $\overline{\mathrm{BHAR}}$ uncertainty. This exercise may even overestimate the influence because $p(\lambda|M_\star, z)$ may bend downward or quickly vanish at very small λ (Aird et al. 2017, 2018). Therefore, the cut at $\log\lambda = 31.5$ is not expected to cause material biases to $\overline{\mathrm{BHAR}}$.

We show our sampled $\overline{\mathrm{BHAR}}$ results in Figure 6, and the $\overline{\mathrm{BHAR}}$ maps will be released online. The median map clearly shows that $\overline{\mathrm{BHAR}}$ increases with both $M_\star$ and z, qualitatively consistent with the conclusions in Yang et al. (2018). The uncertainty map reveals that the $\overline{\mathrm{BHAR}}$ constraints at both the low-z/high-$M_\star$ and the high-z/low-$M_\star$ regime are relatively more limited. We will present a more quantitative comparison with Yang et al. (2018) and other works in Section 4.2. Besides, we verified that AGN-dominated sources do not cause material biases to our $\overline{\mathrm{BHAR}}$ measurements in Appendix D.

There are slight, local fluctuations in $\overline{\mathrm{BHAR}}$ that are caused by the statistical noise of the data and are confined within the extent allowed by our prior, and the $\overline{\mathrm{BHAR}}$ map is smooth globally, as can be seen in the top panel of Figure 6. The fluctuation levels and $\overline{\mathrm{BHAR}}$ uncertainties depend on our prior

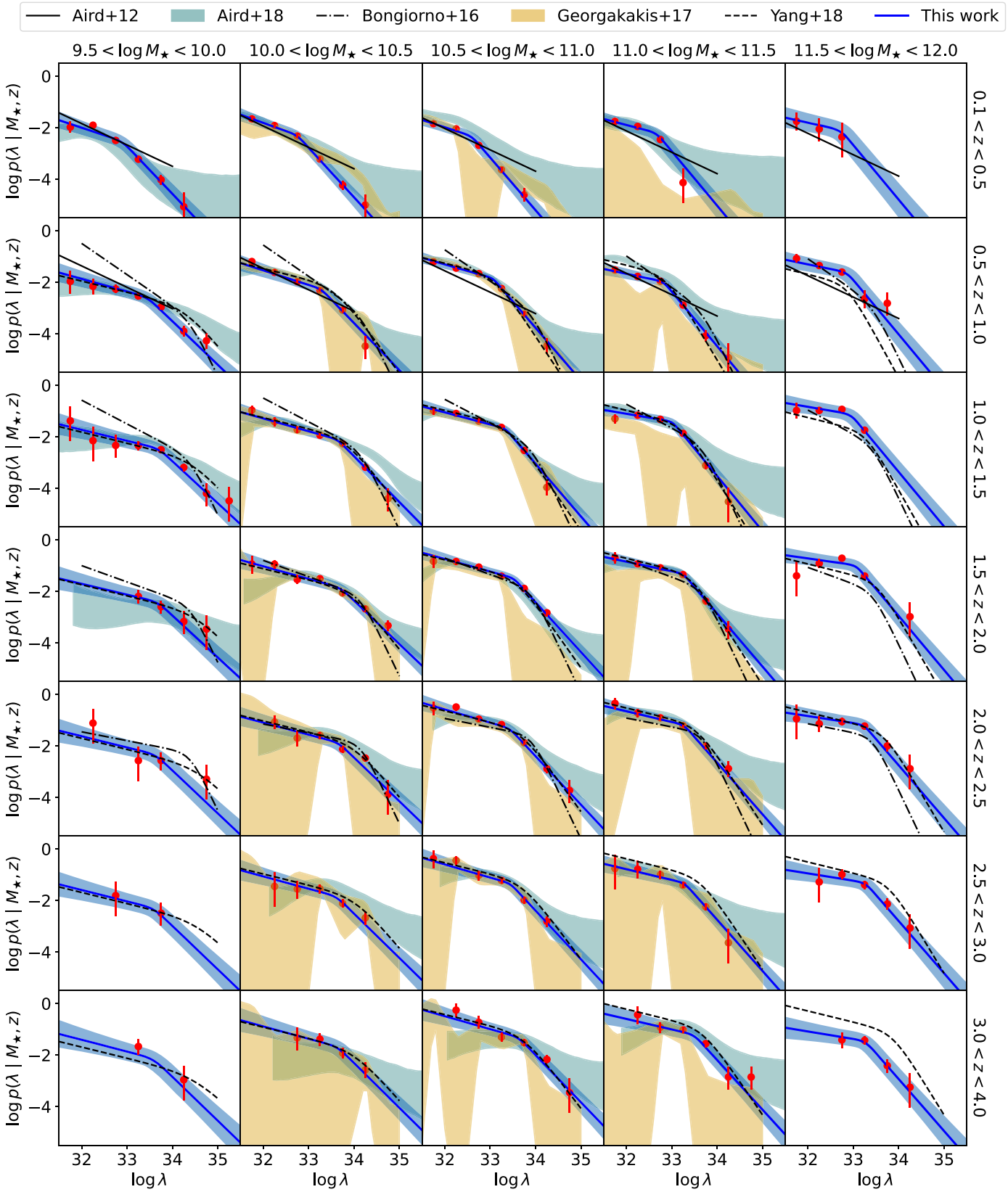

Figure 3. Comparison between our $p(\lambda|M_\star, z)$ and other measurements. The red points are the binned estimators with 1σ error bars based on our data. The blue curves represent our fitted median $p(\lambda|M_\star, z)$, evaluated at the bin centers, and the blue shaded regions represent the corresponding 90% confidence ranges. The black solid straight lines represent the single power-law models in Aird et al. (2012). The dashed–dotted and dashed curves represent the double power-law models in Bongiorno et al. (2016) and Yang et al. (2018), respectively. The cyan and orange-shaded regions denote the 90% confidence intervals of the nonparametric $p(\lambda|M_\star, z)$ in Aird et al. (2018) and Georgakakis et al. (2017), respectively.

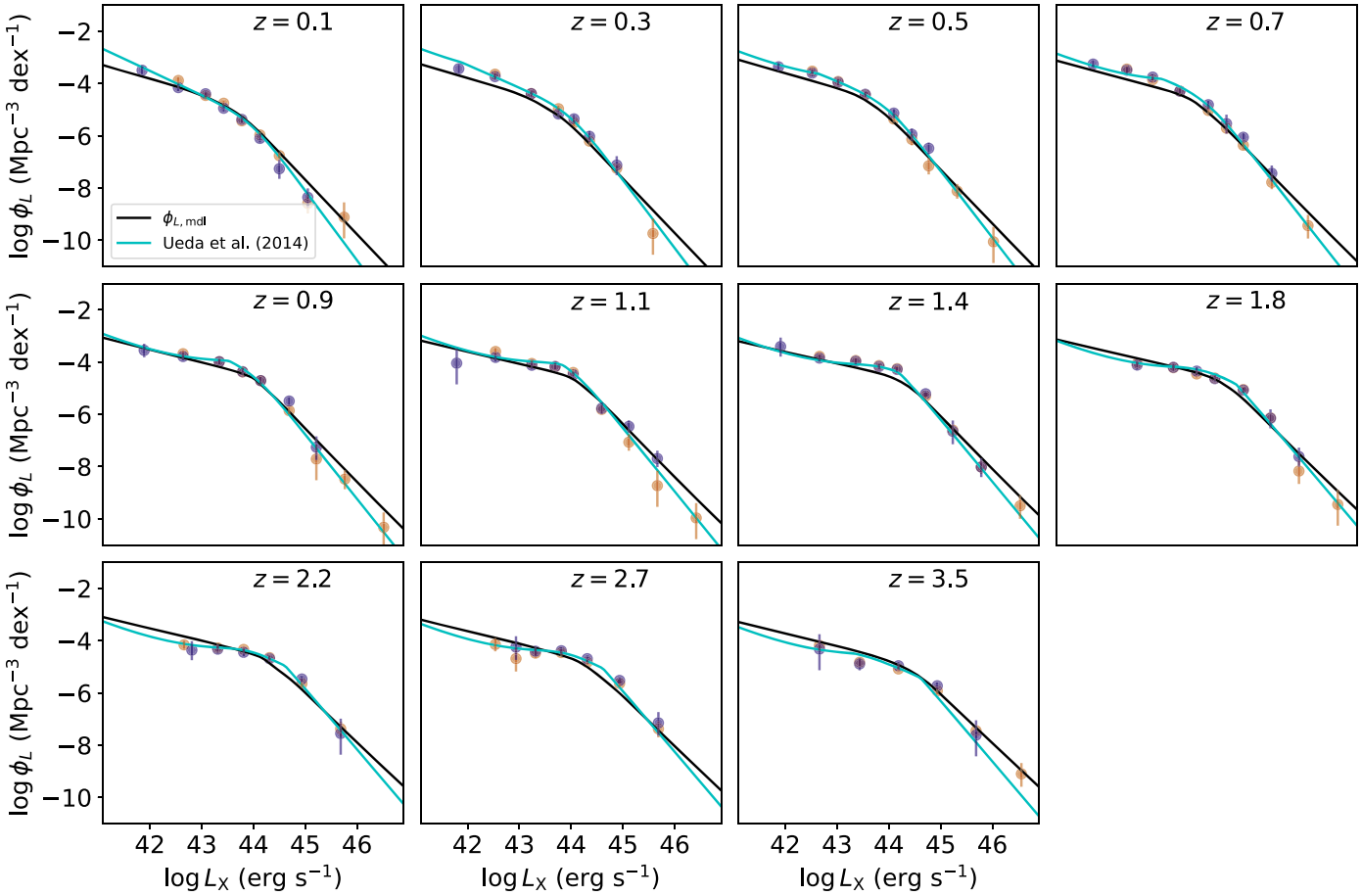

Figure 4. The XLFs at different redshifts. The red (blue) data points indicate the soft-band (HB) XLFs in Ueda et al. (2014). The cyan curves indicate the best-fit XLF models in Ueda et al. (2014), and the black curves denote our $\phi_{L,\mathrm{mdl}}$ based on the median parameter maps in Figure 2 and the SMF in Wright et al. (2018). The absorption correction has been appropriately applied for both our measurements (see Section 3.1.1) and the XLFs in Ueda et al. (2014). Our models agree with the observed XLFs well.

settings but almost not on our bin size because our bins are set to be correlated (Section 3.1.3). For example, relaxing the prior by choosing larger σ_X would return larger fluctuations and uncertainties. This *arbitrariness* is inherent in modeling.[14] Overall, our prior is reasonably constructed (Section 3.1.3) and provides beneficial regularizations. We have assessed the potential issue of whether such arbitrary choices affect the following posterior inferences and the resulting scientific conclusions qualitatively. For example, we have conducted a sensitivity check of our priors and confirmed that the impact of lower or higher resolution of the prior surface (corresponding to larger or smaller bin sizes) does not influence the resulting posterior inference in a noticeable way, and changing σ_X generally would not cause material changes of the median BHAR map.

4. Discussion

Given that this article is already lengthy and full of technical details, we decide to present more scientific investigations of our results in future dedicated works. However, we would like to present brief, immediate, but sufficiently informative explorations of our results in this section, which helps justify the quality and serves as a precursor of further detailed scientific investigations.

[14] For the widely used method of binning the parameter space and assuming each bin is independent, there is a similar arbitrariness in choosing the bin size, and the uncertainties in this case would depend on the bin size.

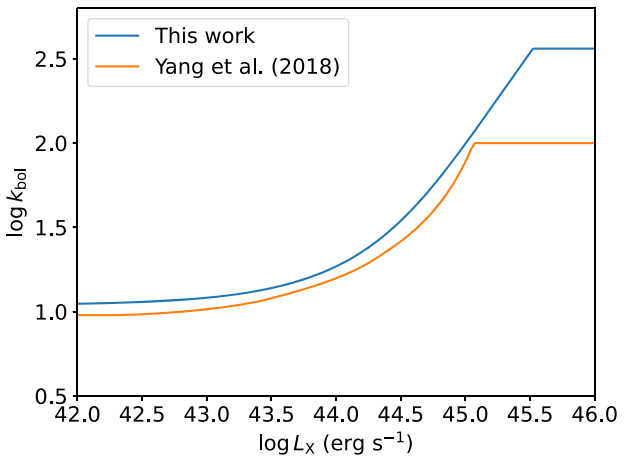

Figure 5. The adopted L_X–k_{bol} relation, taken from Duras et al. (2020). The adopted relation used in Yang et al. (2018), which is adjusted from Lusso et al. (2012), is also plotted for comparison.

4.1. Adding External Constraints from the SMF and XLF

Section 3.2 uses the SMF and XLF to examine the fitting quality of $p(\lambda|M_\star, z)$. It is also possible to follow a reversed

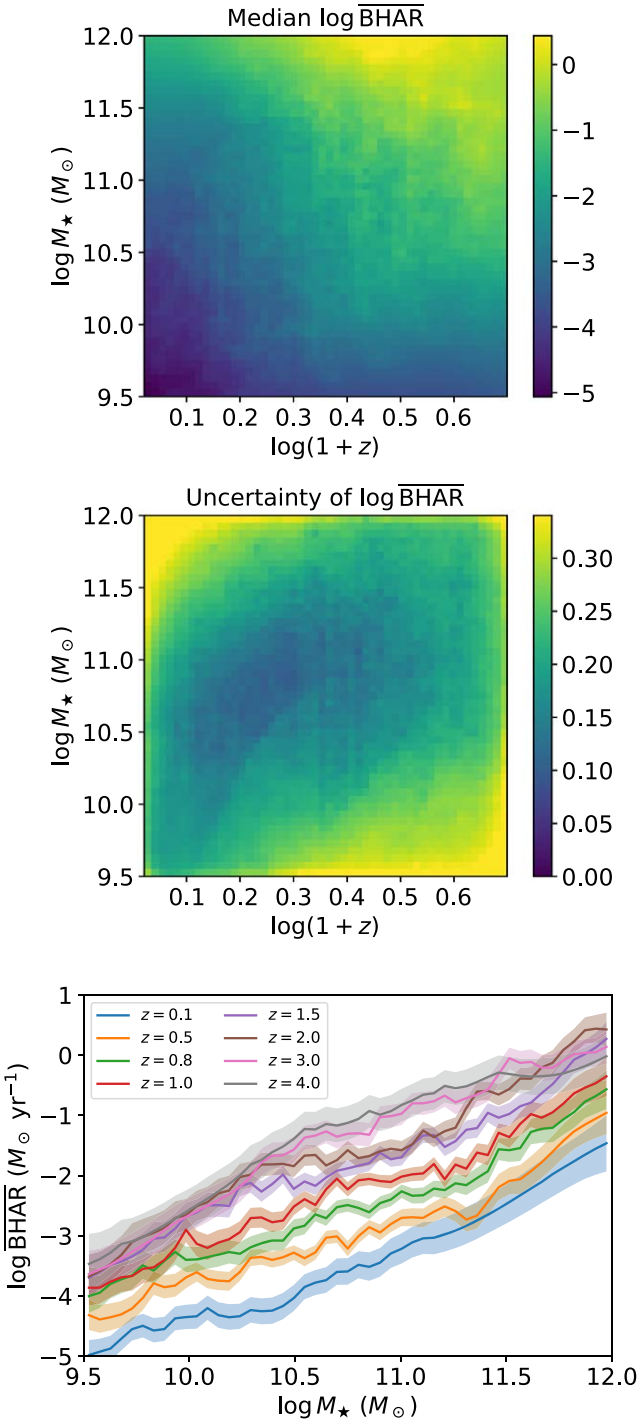

Figure 6. The top and middle panels are the sampled $\overline{\rm BHAR}$ maps, where the unit of $\overline{\rm BHAR}$ is $M_\odot$ yr^{-1}. The bottom panel shows the $\overline{\rm BHAR}$–$M_\star$ relation at several redshifts, where the solid curves represent the median values, and the shaded regions represent the corresponding 1σ uncertainty ranges. $\overline{\rm BHAR}$ generally increases with both $M_\star$ and z.

direction—we can add external constraints from the SMF and XLF (named the *SMF-XLF constraints,* hereafter) into our posterior. This approach was adopted in Yang et al. (2018). As a start, we revisit the numerical computations of $\phi_{L,\rm mdl}$ in Equation (22). Again, numerical integrations should be avoided whenever possible, and we hence derive an analytical formula for $\phi_{L,\rm mdl}$. ϕ_M is expressed as a two-component Schechter function in Wright et al. (2018):

$$\phi_M = \frac{dn}{d\log M_\star} = \ln 10\, e^{-\frac{M_\star}{M_c}}\left[\phi_1\left(\frac{M_\star}{M_c}\right)^{\alpha_1+1} + \phi_2\left(\frac{M}{M_c}\right)^{\alpha_2+1}\right], \tag{23}$$

where (M_c, α_1, α_2, ϕ_1, ϕ_2) are redshift-dependent parameters. We further define an auxiliary function ψ such that the model-predicted XLF in Equation (22) can be simplified as summations of ψ (see below).

$$\begin{aligned}
&\psi(\gamma, M_1, M_2, A, \lambda_c; L_{\rm X})\\
&= \int_{\log M_1}^{\log M_2} A\left(\frac{L_{\rm X}}{M_\star \lambda_c}\right)^{-\gamma} \phi_M d\log M_\star\\
&= A\left(\frac{L_{\rm X}}{M_\star \lambda_c}\right)^{-\gamma}\left[\phi_1 \Gamma_{\rm GI}\left(\alpha_1+\gamma+1, \frac{M_1}{M_c}, \frac{M_2}{M_c}\right)\right.\\
&\left. + \phi_2 \Gamma_{\rm GI}\left(\alpha_2+\gamma+1, \frac{M_1}{M_c}, \frac{M_2}{M_c}\right)\right],
\end{aligned} \tag{24}$$

where $\Gamma_{\rm GI}(\zeta, x_1, x_2) = \int_{x_1}^{x_2} t^{\zeta-1}e^{-t}dt$ is the generalized incomplete Gamma function. The contribution of each grid element to the integration in Equation (22) is

$$\begin{aligned}
&\psi_{\rm DP}(A, \lambda_c, \gamma_1, \gamma_2, M_1, M_2; L_{\rm X})\\
&= \int_{\log M_1}^{\log M_2} p(L_{\rm X}/M_\star | M_\star, z)\phi_M d\log M_\star\\
&= \begin{cases}
\psi(\gamma_2, M_1, M_2, A, \lambda_c; L_{\rm X}), & \lambda_c \leqslant L_{\rm X}/M_2\\
\psi(\gamma_2, M_1, L_{\rm X}/\lambda_c, A, \lambda_c; L_{\rm X})\\
+\ \psi(\gamma_1, L_{\rm X}/\lambda_c, M_2, A, \lambda_c; L_{\rm X}), & L_{\rm X}/M_2 < \lambda_c < L_{\rm X}/M_1,\\
\psi(\gamma_1, M_1, M_2, A, \lambda_c; L_{\rm X}), & \lambda_c \geqslant L_{\rm X}/M_1
\end{cases}
\end{aligned} \tag{25}$$

Equation (22) is thus

$$\phi_{L,\rm mdl} = \sum_{i=1}^{N_M} \psi_{\rm DP}(A_{ij_z}, \lambda_{c,ij_z}, \gamma_{1,ij_z}, \gamma_{2,ij_z}, M_{LB,i}, M_{LB,i+1}; L_{\rm X}), \tag{26}$$

where $\log M_{LB,i} = \log M_{\star,\min} + (i-1)/N_M \times \log(M_{\star,\max}/M_{\star,\min})$ is the lower bound of the ith $M_\star$-grid element, and j_z is the index of the z-grid element containing z.

We then follow the procedure in Yang et al. (2018) to compare $\phi_{L,\rm mdl}$ and $\phi_{L,\rm obs}$ in Ueda et al. (2014). $\phi_{L,\rm obs}$ is evaluated at several ($L_{\rm X}$, z) values, and the number of sources ($n^{\rm XLF}$) in Ueda et al. (2014) contributing to $\phi_{L,\rm obs}$ is recorded. Following Yang et al. (2018), we use the soft-band XLF at $L_{\rm X} > 10^{43}$ erg s^{-1} in Ueda et al. (2014). Their soft-band XLF has been corrected for obscuration and spans a wider $L_{\rm X}$ range compared to their HB XLF, and their soft-band and HB XLFs are also consistent (see Figure 4). The $L_{\rm X}$ cut at 10^{43} erg s^{-1} is adopted to avoid contamination from X-ray binaries. The log-

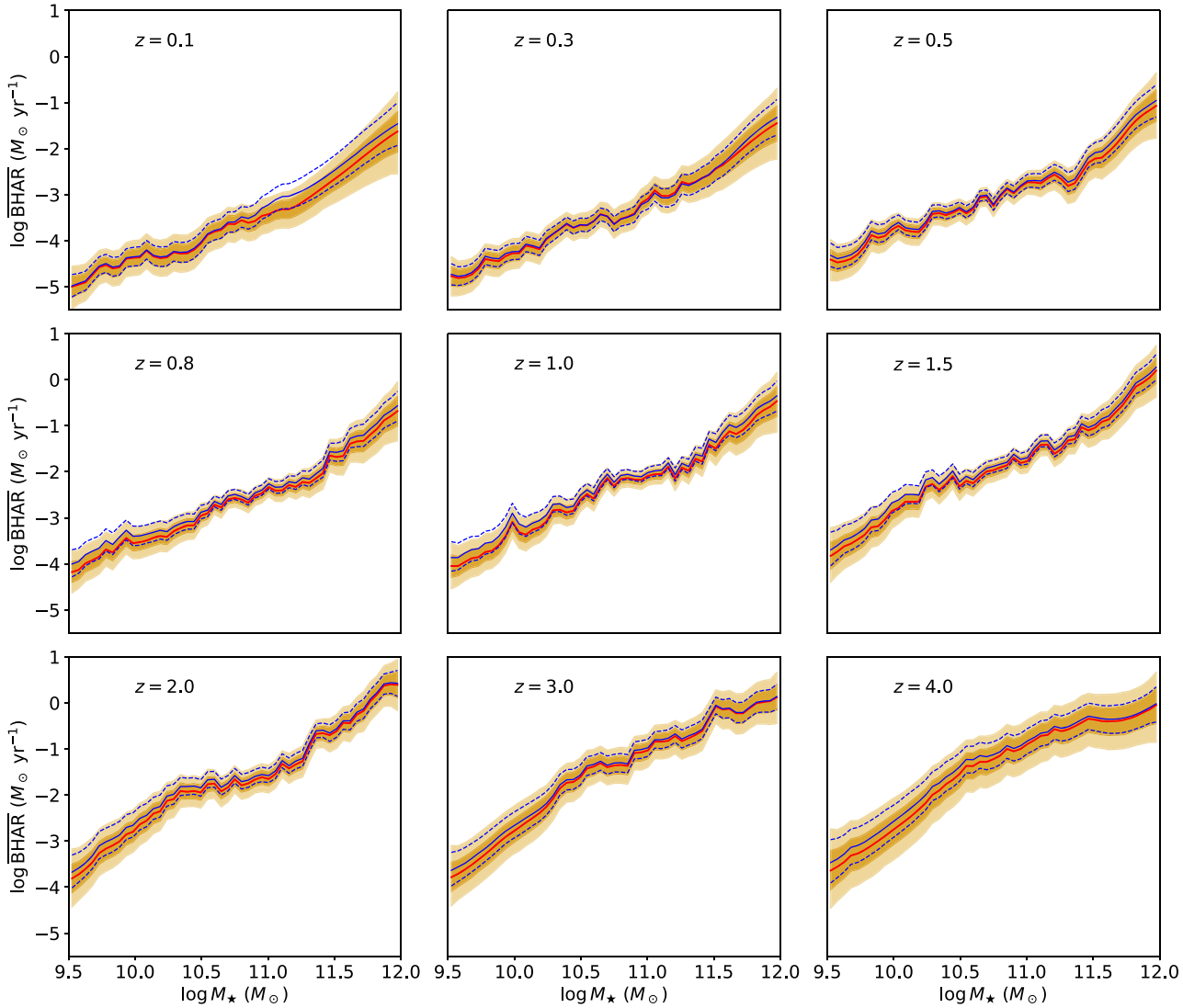

Figure 7. $\overline{\mathrm{BHAR}}$ as a function of $M_\star$ at several redshifts. The red curves represent our median $\overline{\mathrm{BHAR}}$ with the SMF-XLF constraints added, and the orange-shaded regions represent the corresponding 1σ and 2σ uncertainty ranges. The blue curves represent our median $\overline{\mathrm{BHAR}}$ and 1σ uncertainties without the SMF-XLF constraints.

likelihood when comparing $\phi_{L,\mathrm{mdl}}$ and $\phi_{L,\mathrm{obs}}$ is

$$\ln \mathcal{L}_{\mathrm{SMF-XLF}} = \sum_k \ln \mathrm{Pr}\left(\mathrm{Poisson}\left(\frac{\phi_{L,\mathrm{mdl},k}}{\phi_{L,\mathrm{obs},k}} n_k^{\mathrm{XLF}}\right) = n_k^{\mathrm{XLF}}\right)$$
$$= \sum_k n_k^{\mathrm{XLF}} \left[\ln\left(\frac{\phi_{L,\mathrm{mdl},k}}{\phi_{L,\mathrm{obs},k}}\right) - \frac{\phi_{L,\mathrm{mdl},k}}{\phi_{L,\mathrm{obs},k}}\right] + \mathrm{const.}, \quad (27)$$

$$\phi_{L,\mathrm{mdl},k} = \phi_{L,\mathrm{mdl}}(L_{\mathrm{X},k}, z_k), \quad (28)$$

where k runs over all the L_{X} and z bins of the observed XLF in Ueda et al. (2014). This term is called the SMF-XLF likelihood in Yang et al. (2018).

To add the SMF-XLF constraints, Equation (20) should be modified as follows:

$$\ln \mathcal{P} = \sum_{\mathrm{field}} \ln \mathcal{L} + \ln \mathcal{L}_{\mathrm{SMF-XLF}} + \ln \pi_{\mathrm{cont}}. \quad (29)$$

Its gradient is presented in Appendix B for HMC sampling. We then sample the above posterior with HMC and present the resulting $\overline{\mathrm{BHAR}}$ in Figure 7. The $\overline{\mathrm{BHAR}}$ curves with or without the SMF-XLF constraints are largely consistent with a small ($<1\sigma$) difference. This is expected because Figure 4 shows that our $\overline{\mathrm{BHAR}}$ without the SMF-XLF constraints leads to consistent XLFs with those in Ueda et al. (2014).

Although there is good consistency after adding the SMF-XLF constraints in our case, extra cautions are generally needed. The SMF and XLF taken from other literature works usually involve inherent assumptions about their parametric forms. When putting the SMF and XLF into our posterior, we will inevitably *absorb* these assumptions. Besides, the original data used to measure the XLF may overlap with one's data set, especially given that the X-ray data in GOODS-S are also necessary to constrain the XLF at low-L_{X} and/or high-z. Such an overlap causes double counting of the involved sources. Especially, more considerations would be needed if the posterior is dominated by the SMF-XLF constraints.

4.2. Comparison with Previous Works

Figure 3 compares our $p(\lambda|M_\star, z)$ with some representative results in previous literature. (Aird et al. 2012; black solid lines in Figure 3) used a single power law to fit $p(L_{\mathrm{X}}|M_\star, z)$ at $z < 1$,

which is converted to a single power law $p(\lambda|M_\star, z)$ in Figure 3. The single power-law curves broadly follow our double power-law ones, and the single power-law index lies within the range between γ_1 and γ_2. This indicates that a single power-law model can serve well as the first-order approximation of $p(\lambda|M_\star, z)$, as has been widely adopted in other works (e.g., Bongiorno et al. 2012; Wang et al. 2017; Birchall et al. 2020, 2023; Zou et al. 2023), especially when the data are limited. However, the real $p(\lambda|M_\star, z)$ is more complicated, and a double power-law model can return better characterizations. As Figure 3 shows, the binned $p(\lambda|M_\star, z)$ estimators generally do not show systematic deviations from our double power-law curves (e.g., no further breaks are visible), and thus a double power-law model is sufficient to capture the main structures of $p(\lambda|M_\star, z)$ at $\lambda > \lambda_{\rm min}$.

Bongiorno et al. (2016) and Yang et al. (2018) adopted a double power-law model similar to ours, and we plot their results as the dashed–dotted and dashed lines in Figure 3, respectively. Our $p(\lambda|M_\star, z)$ curves are nearly identical to those in Yang et al. (2018) at $10 \lesssim \log M_\star \lesssim 11.5$ and $1 \lesssim z \lesssim 2.5$ but begin diverging in other parameter ranges. In the lowest-mass bin ($9.5 < \log M_\star < 10$), our $p(\lambda|M_\star, z)$ is still similar to those in Yang et al. (2018) at $\log \lambda \lesssim 33.5$ but is lower than theirs at higher λ. In the highest-mass bin ($11.5 < \log M_\star < 12$), our $p(\lambda|M_\star, z)$ is larger at $z \lesssim 2$ and smaller at $z \gtrsim 2$ than for Yang et al. (2018). It should be noted that these parameter regions with noticeable $p(\lambda|M_\star, z)$ differences generally have limited data and are far away from the bulk of other data points, and the results in these regions are subject to large uncertainties. For Bongiorno et al. (2016), their $p(\lambda|M_\star, z)$ is similar to ours at $10 \lesssim \log M_\star \lesssim 11.5$ and $1.5 \lesssim z \lesssim 2$ but has a much steeper low-λ power-law index at $z < 1.5$. Two reasons may be responsible for the difference—the data used in Bongiorno et al. (2016) are not sufficiently deep to effectively probe the low-λ regime; their model always fixes the break-point at $\log \lambda = 33.8$ when $M_\star = 10^{11}\, M_\odot$, while our results suggest that the breakpoint tends to become smaller as redshift decreases.

Georgakakis et al. (2017) and Aird et al. (2018) adopted nonparametric methods to measure $p(\lambda|M_\star, z)$ without assuming a double power-law form. Our results show good agreement with theirs, especially in regimes well covered by the data, suggesting that a double power-law is indeed a good approximation of $p(\lambda|M_\star, z)$. Nonetheless, some differences are worth noting. At $\log \lambda \gtrsim 34$ where the data become limited, the $p(\lambda|M_\star, z)$ in Aird et al. (2018) tends to be flatter than ours, while that in Georgakakis et al. (2017) tends to be steeper than ours. This high-λ regime is highly uncertain and subject to the adopted methodology—for instance, the prior adopted in Aird et al. (2018) prefers a flatter slope at high λ. Another feature is that the $p(\lambda|M_\star, z)$ in Aird et al. (2018) sometimes shows downward bending at $\log \lambda \approx 32$–33, while that in Georgakakis et al. (2017) does not show a clear bending, although the large uncertainty may be responsible for the lack of bending. In principle, a downward bending at some low λ is expected; otherwise, $p(\lambda|M_\star, z)$ would diverge. Such bending can also be seen in Georgakakis et al. (2017), but below $\log \lambda_{\rm min} = 31.5$ (see, e.g., their Figure 7). Our double power-law model is unable to capture this feature, and Figure 3 shows that the bending in Aird et al. (2018) mainly becomes prominent at high redshift ($z \gtrsim 3$).

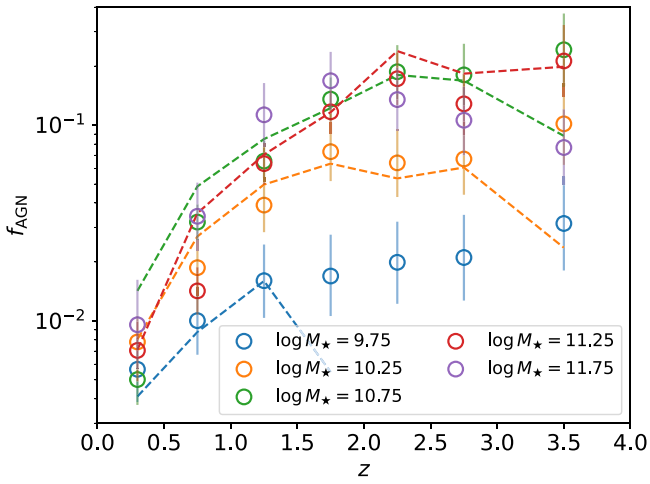

Figure 8. $f_{\rm AGN}$ evaluated at several $(M_\star, z)$ values vs. z. Our results are plotted as open circles with 1σ error bars, where different colors represent different $M_\star$. The dashed lines denote those in Aird et al. (2018).

Another metric that can be measured from $p(\lambda|M_\star, z)$ is the fraction of galaxies hosting accreting SMBHs above a given λ threshold ($\lambda_{\rm thres}$), as calculated below

$$f_{\rm AGN}(\lambda > \lambda_{\rm thres}) = \int_{\log \lambda_{\rm thres}}^{+\infty} p(\lambda|M_\star, z) d \log \lambda. \quad (30)$$

For a consistent comparison with Aird et al. (2018), we adopt the same $\lambda_{\rm thres} = 32$ as theirs. We calculate $f_{\rm AGN}$ at several $(M_\star, z)$ values and plot the results in Figure 8. Our results generally agree well with those in Aird et al. (2018) and follow similar evolutionary trends with respect to $M_\star$ and z. At $\log M_\star \gtrsim 10$, $f_{\rm AGN}$ increases with z up to $z \approx 1.5$–2 and reaches a plateau at higher redshift; while for less-massive galaxies, the redshift evolution is weaker. At low redshift ($z \lesssim 0.5$), $f_{\rm AGN}$ is similar regardless of $M_\star$, and this conclusion can be further extended down to $\log M_\star < 9.5$, as Zou et al. (2023) showed that the λ-based $f_{\rm AGN}$ in the dwarf galaxy population in this redshift range is also similar to $f_{\rm AGN}$ in massive galaxies. At higher redshift ($z \gtrsim 1$), the dependence of $f_{\rm AGN}$ on $M_\star$ becomes more apparent due to $M_\star$-dependent redshift evolution rates of $f_{\rm AGN}$, and there is a positive correlation between $f_{\rm AGN}$ and $M_\star$ at $\log M_\star \lesssim 10.5$. However, for massive galaxies with $\log M_\star \gtrsim 10.5$, $f_{\rm AGN}$ nearly does not depend on $M_\star$. A full physical explanation of these complicated correlations between $f_{\rm AGN}$ and $(M_\star, z)$ will require further detailed analyses of $p(\lambda|M_\star, z)$ with at least partially physically driven modeling, and we leave these analyses for future work.

We further compare our $\overline{\rm BHAR}$ with those in Yang et al. (2018) in Figure 9. Our median relation is largely similar to theirs, but some subtle differences exist. Our low-mass $\overline{\rm BHAR}$ at $\log M_\star \lesssim 10$ is slightly smaller across all redshifts, though not very significant. Our high-mass $\overline{\rm BHAR}$ at $\log M_\star \gtrsim 11.5$ differs the most from that in Yang et al. (2018), and ours tends to be smaller at $z \gtrsim 3$ while being larger at $z \lesssim 2$. These differences originate from different $p(\lambda|M_\star, z)$, as discussed earlier in this section. As shown in Figure 3, our low-mass $p(\lambda|M_\star, z)$ is smaller than for Yang et al. (2018) only at high λ, and thus the low-mass $\overline{\rm BHAR}$ difference is small. Our high-mass $p(\lambda|M_\star, z)$ at $\log M_\star \gtrsim 11.5$, instead, shows a redshift-dependent difference in the normalization. Nevertheless, the

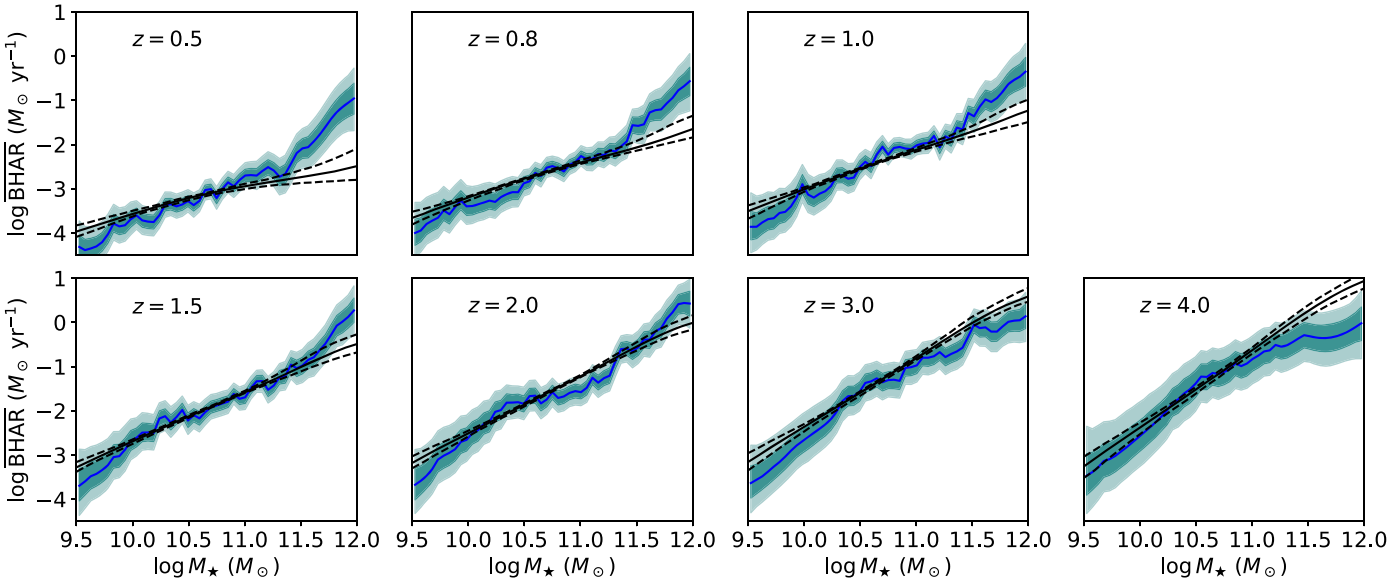

Figure 9. The comparison of our $\overline{\mathrm{BHAR}}$ with those in Yang et al. (2018). The blue curves represent our median $\overline{\mathrm{BHAR}}$, and the cyan-shaded regions represent the corresponding 1σ and 2σ uncertainty ranges. The $\overline{\mathrm{BHAR}}$ and the corresponding 1σ uncertainty in Yang et al. (2018) are plotted as the black curves.

uncertainties in these extreme regimes are large, and they are also subject to model choices. Dedicated analyses of these extreme-mass sources with deeper or wider data may be necessary to further pin down the uncertainty. Another important difference is that the $\overline{\mathrm{BHAR}}$–$M_\star$ relation in Yang et al. (2018) flattens at low redshift, but ours does not show such a trend. Therefore, the $\overline{\mathrm{BHAR}}$ in Yang et al. (2018) is less reliable at $z \lesssim 0.8$, as they noted; if their relation is further extrapolated below $z = 0.5$, their $\overline{\mathrm{BHAR}}$–$M_\star$ relation would become flat and is thus unphysical. Our $\overline{\mathrm{BHAR}}$ uncertainties are also considerably larger than those in Yang et al. (2018), even though we used more data. This is because Yang et al. (2018) adopted a parametric modeling method, which includes strong a priori assumptions. In contrast, this work minimizes such assumptions, and thus the fitted uncertainties reflect those directly inherited from the data.

4.3. Star-forming versus Quiescent Galaxies

Star-forming galaxies generally have stronger AGN activity than quiescent galaxies (e.g., Aird et al. 2018, 2019). We hence examine if star-forming and quiescent galaxies have the same $\overline{\mathrm{BHAR}}$ in this section.

To separate star-forming and quiescent galaxies, we adopt the star-forming main sequence (MS) in Popesso et al. (2023) and define quiescent galaxies as those lying at least 1 dex below the MS; the remaining galaxies are star-forming ones. Since the star-forming and quiescent subpopulations do not individually follow the SMF and XLF, we do not apply the SMF-XLF constraints as in Section 4.1. We measure their $\overline{\mathrm{BHAR}}$ and present the results in Figure 10. The $\overline{\mathrm{BHAR}}$ of both star-forming and quiescent galaxies increases with $M_\star$ and z. When comparing the $\overline{\mathrm{BHAR}}$ of these two subpopulations, star-forming galaxies generally have larger $\overline{\mathrm{BHAR}}$, suggesting that star-forming galaxies indeed host more active SMBHs, possibly due to more available cold gas for both star formation and SMBH accretion. The $\overline{\mathrm{BHAR}}$ difference between the two populations also depends on $M_\star$ and z. At $\log M_\star \lesssim 10.5$, the difference is generally small across most of the redshift range. At higher mass, the difference is small at low redshift but becomes apparent when z increases to 1 and further decreases at higher redshift. There is also tentative evidence suggesting that the redshift at which the difference reaches its peak might also shift with $M_\star$, with the peak of the $\overline{\mathrm{BHAR}}$ difference of higher-mass galaxies occurring at higher redshift.

One caveat that should be noted is that our results depend on the classification between star-forming and quiescent galaxies. Such a classification is more reliable at $M_\star \lesssim 10^{10.5}\,M_\odot$, but it may become sensitive to the adopted method at higher $M_\star$ and lower z (e.g., Donnari et al. 2019). Cristello et al. (2024) show that the star-forming and quiescent subpopulations cannot be safely defined for massive galaxies, and Feldmann (2017) also argued that the bimodal separation is not necessarily appropriate. The proposed redshift-dependent maximum $M_\star$ values for reliable classifications in Cristello et al. (2024) can be well described by the following equation:

$$\log M_\star = 10.65 + 0.81\log(z) + 0.83\log(1+z), \quad (31)$$

and they are explicitly plotted in Figure 10. We also plot the $\overline{\mathrm{BHAR}}$ of the whole population in Figure 10, and it is similar to the star-forming $\overline{\mathrm{BHAR}}$ below the $M_\star$ threshold in Equation (31) and becomes more in the middle between the star-forming and quiescent $\overline{\mathrm{BHAR}}$ with rising $M_\star$. Therefore, Equation (31) can also serve as an approximate threshold of whether the contribution of the SMBH growth in quiescent galaxies to the overall SMBH growth is important.

Our results suggest that the $\overline{\mathrm{BHAR}}(M_\star, z)$ function may also depend on SFR, with star-forming galaxies hosting enhanced AGN activity (e.g., Aird et al. 2018, 2019; Birchall et al. 2023). However, such a dependence is only secondary (Yang et al. 2017), and SFR is usually more challenging to measure and more subject to confusion with AGN emission. Still, more physical insights can be gained by incorporating SFR-based parameters, especially when probing $p(\lambda|M_\star, z)$ instead of $\overline{\mathrm{BHAR}}$ (Aird et al. 2018). We leave further analyses on including SFR into the $\overline{\mathrm{BHAR}}(M_\star, z)$ function to the future, in which different classification schemes from binary (star-forming versus quiescent) up to four categories (starburst, star-forming, transitioning, and quiescent) will be explored.

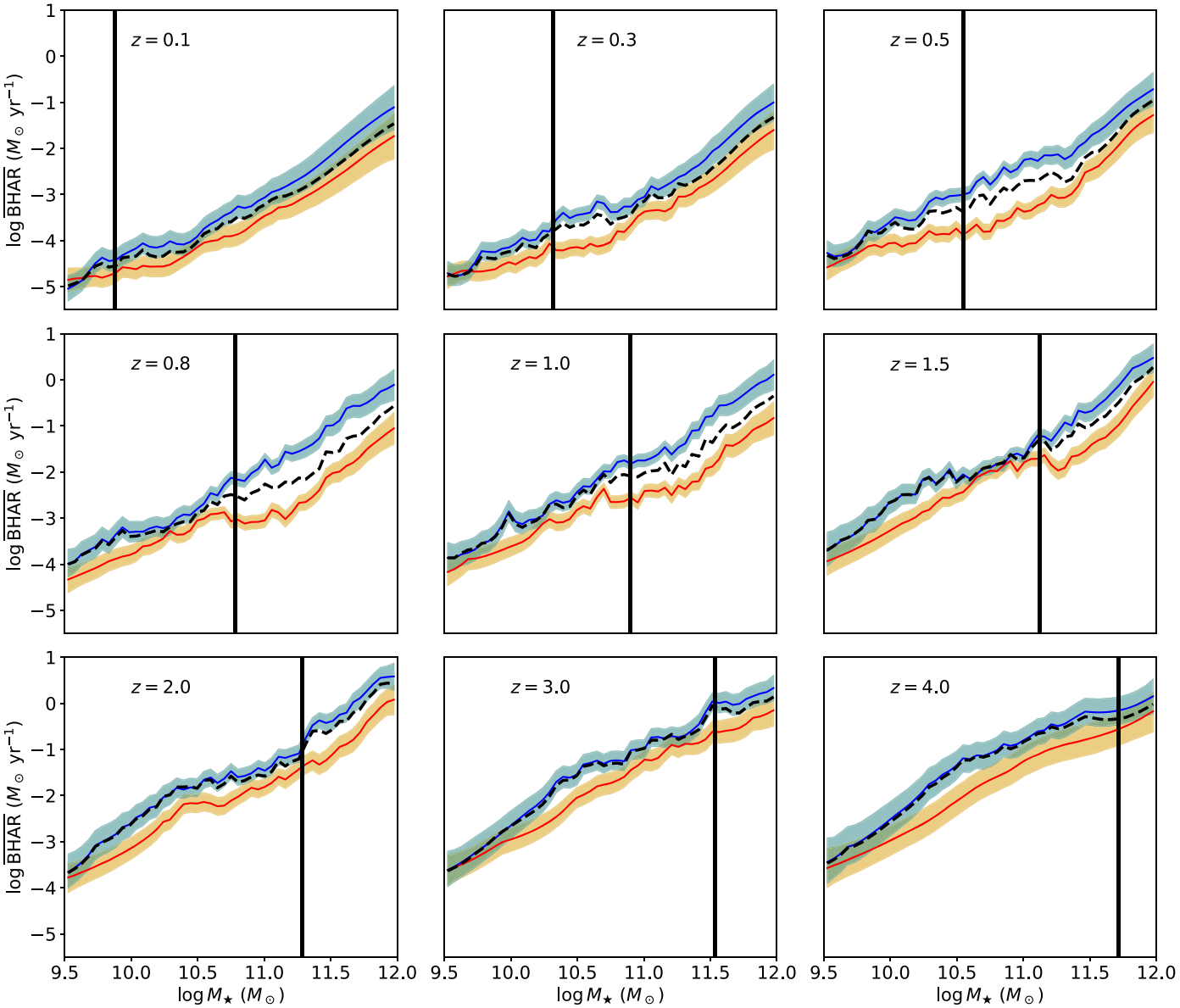

Figure 10. $\overline{\mathrm{BHAR}}$ for star-forming (blue) and quiescent (red) galaxies. The shaded regions represent 1σ uncertainty ranges. The black dashed curves denote the $\overline{\mathrm{BHAR}}$ with all the galaxies included, i.e., those in Figure 6. The vertical black lines mark the maximum $M_\star$ values where star-forming and quiescent galaxies can be reliably classified at the corresponding z (Cristello et al. 2024). Star-forming galaxies have larger $\overline{\mathrm{BHAR}}$.

5. Summary and Future Work

In this work, we mapped $\overline{\mathrm{BHAR}}$ as a function of ($M_\star$, z) over the vast majority of cosmic time, and our main results are summarized as follows:

1. We compiled an unprecedentedly large sample from nine fields—CANDELS (including GOODS-S, GOODS-N, EGS, and UDS), the LSST DDFs (including COSMOS, ELAIS-S1, W-CDF-S, and XMM-LSS), and eFEDS. These fields include both deep, small-area surveys and shallow, large-area ones. The former provides rich information in the high-z, low-$M_\star$, and/or low-λ regime, while the latter provides complementary information in the low-z, high-$M_\star$, and/or high-λ regime. Therefore, our sample can effectively constrain $\overline{\mathrm{BHAR}}$ across a large range of the relevant parameter space. See Section 2.
2. We developed a semiparametric Bayesian method to measure $\overline{\mathrm{BHAR}}$, where a double power-law model with respect to λ is used to measure $p(\lambda|M_\star, z)$, and the relevant parameters nonparametrically depend on ($M_\star$, z). This method has two main advantages. It avoids the *extrapolation* of parameters from well-populated regions in the parameter space to less-populated regions. It also adopts much weaker assumptions than parametric methods, enabling more flexible constraints and more representative fitting uncertainties from the data. See Section 3.1.
3. We sampled $p(\lambda|M_\star, z)$ and measured $\overline{\mathrm{BHAR}}$ at $10^{9.5} < M_\star < 10^{12}\,M_\odot$ and $z < 4$. We have verified the fitting quality by comparing our model $p(\lambda|M_\star, z)$ and the corresponding binned estimators and also by comparing our inferred XLF with the observed one. We showed that

$\overline{\mathrm{BHAR}}$ increases with both $M_\star$ and z. Our $\overline{\mathrm{BHAR}}$ measurements are largely consistent with those in Yang et al. (2018) at $z \gtrsim 0.8$, and we also, for the first time, provide reasonable constraints upon $\overline{\mathrm{BHAR}}$ at lower redshift ($z \lesssim 0.5$). See Sections 3.2 and 3.3.

4. We measured $\overline{\mathrm{BHAR}}$ for both star-forming, and for the first time, quiescent galaxies. Both groups show $\overline{\mathrm{BHAR}}$ increases with $M_\star$ and z, and the star-forming $\overline{\mathrm{BHAR}}$ is generally larger than or at least comparable to the quiescent $\overline{\mathrm{BHAR}}$ across the whole ($M_\star$, z) plane. See Section 4.3.

It should be noted that, besides $\overline{\mathrm{BHAR}}$, our $p(\lambda|M_\star, z)$ parameter maps in Figure 2 also contain rich information, and we release $p(\lambda|M_\star, z)$ and the corresponding parameter maps and $\overline{\mathrm{BHAR}}$ maps in Zenodo, doi:10.5281/zenodo.10729248. As first examples, we have briefly and phenomenologically discussed different scientific questions in Sections 4.2 and 4.3, which justified that our results can reveal interesting dependences of SMBH growth on the galaxy population.

Figure 3 visually illustrates that $p(\lambda|M_\star, z)$ evolves over ($M_\star$, z). Observationally, it is still unclear what the exact evolution pattern is, let alone the physics driving such an evolution. It is also unknown from a theoretical perspective because no simulations appear to produce consistent evolution patterns of $p(\lambda|M_\star, z)$ with the observed ones (e.g., Habouzit et al. 2022). It even complicates matters further that $p(\lambda|M_\star, z)$ may evolve differently for star-forming and quiescent galaxies, as proposed in a phenomenological scenario in Aird et al. (2018). We leave detailed analyses of the $p(\lambda|M_\star, z)$ evolution to a subsequent future work. We will first identify the qualitative evolution pattern of the dependence of $p(\lambda|M_\star, z)$ on $M_\star$ and z for different galaxy populations and then develop a quantitative, parametric model to depict the identified evolution pattern. With the clearly understood $p(\lambda|M_\star, z)$, we will address the following scientific questions. Is the broad decline in SMBH growth below $z \approx 1$ due to the shift of accretion activity to smaller galaxies or a reduction of the typical λ? How large is the AGN *duty cycle*, which is an integration of $p(\lambda|M_\star, z)$, in different galaxy populations? Does $M_\star$ modulate the duty cycle or modulate the typical outburst luminosity in the AGN phase? Is there any difference in the SMBH feeding in star-forming and quiescent galaxies?

Acknowledgments

We thank the anonymous referee for constructive suggestions and comments. We thank Nathan Cristello, Joel Leja, and Zhenyuan Wang for their helpful discussions. F.Z., Z.Y., and W.N.B. acknowledge financial support from NSF grant AST-2106990, Chandra X-ray Center grant AR1-22006X, the Penn State Eberly Endowment, and Penn State ACIS Instrument Team Contract SV4-74018 (issued by the Chandra X-ray Center, which is operated by the Smithsonian Astrophysical Observatory for and on behalf of NASA under contract NAS8-03060). G.Y. acknowledges funding from the Netherlands Research School for Astronomy (NOVA). The Chandra ACIS Team Guaranteed Time Observations (GTO) utilized were selected by the ACIS Instrument Principal Investigator, Gordon P. Garmire, currently of the Huntingdon Institute for X-ray Astronomy, LLC, which is under contract to the Smithsonian Astrophysical Observatory via Contract SV2-82024.

Appendix A
Gradient of the Posterior

This appendix presents the gradient of our posterior in Equation (20). We found that, at least in our case, analytical differentiation enables a much higher computational speed and/or less memory compared with other differentiation algorithms. We thus adopt the analytically derived gradient and directly present the derivation results below.

First, the partial derivatives of $I(\gamma, \lambda_1, \lambda_2, A, \lambda_c; M_\star, z)$ in Equation (12) are

$$\frac{\partial I}{\partial A} = \frac{I}{A}, \tag{A1}$$

$$\frac{\partial I}{\partial \lambda_c} = \frac{\gamma}{\lambda_c} I, \tag{A2}$$

$$\begin{aligned}
\frac{\partial I}{\partial \gamma} =& -\frac{A}{2\gamma \ln 10}\left[\ln\left(\frac{\lambda_1}{\lambda_c}\right) + \frac{1}{\gamma}\right]\left(\frac{\lambda_1}{\lambda_c}\right)^{-\gamma}[\mathrm{erf}(x_1) + 1] \\
&+ \frac{A}{2\gamma \ln 10}\left[\ln\left(\frac{\lambda_2}{\lambda_c}\right) + \frac{1}{\gamma}\right]\left(\frac{\lambda_2}{\lambda_c}\right)^{-\gamma}[\mathrm{erf}(x_2) + 1] \\
&+ \frac{A}{2\gamma \ln 10}\left(\frac{10^{a-\frac{\gamma \ln 10}{4b^2}}}{\lambda_c M_\star \eta}\right)^{-\gamma}\left[\ln\left(\frac{10^a}{\lambda_c M_\star \eta}\right) - \frac{\gamma(\ln 10)^2}{2b^2} + \frac{1}{\gamma}\right] \\
&\times \left[\mathrm{erf}\left(x_1 + \frac{\gamma \ln 10}{2b}\right) - \mathrm{erf}\left(x_2 + \frac{\gamma \ln 10}{2b}\right)\right] \\
&- \frac{A}{2\sqrt{\pi}\gamma b}\left(\frac{10^{a-\frac{\gamma \ln 10}{4b^2}}}{\lambda_c M_\star \eta}\right)^{-\gamma} \\
&\times \left[\exp\left(-\left(x_1 + \frac{\gamma \ln 10}{2b}\right)^2\right) - \exp\left(-\left(x_2 + \frac{\gamma \ln 10}{2b}\right)^2\right)\right]
\end{aligned} \tag{A3}$$

$$\begin{aligned}
\frac{\partial I}{\partial \lambda_k} =& (2k - 3) \\
&\times \left\{\frac{A}{2\lambda_k \ln 10}\left(\frac{\lambda_k}{\lambda_c}\right)^{-\gamma}[\mathrm{erf}(x_k) + 1]\right. \\
&- \frac{Ab}{\sqrt{\pi}(\ln 10)^2 \gamma \lambda_k}\left(\frac{\lambda_k}{\lambda_c}\right)^{-\gamma}\exp(-x_k^2) \\
&\left. + \frac{Ab}{\sqrt{\pi}(\ln 10)^2 \gamma \lambda_k}\left(\frac{10^{a-\frac{\gamma \ln 10}{4b^2}}}{\lambda_c M_\star \eta}\right)^{-\gamma}\exp\left(-\left(x_k + \frac{\gamma \ln 10}{2b}\right)^2\right)\right\} \\
&(k = 1, 2).
\end{aligned} \tag{A4}$$

Defining $\ln p(\lambda; A, \lambda_c, \gamma_1, \gamma_2)$ as $\ln p(\lambda|M_\star, z)$, its partial derivatives are

$$\frac{\partial \ln p}{\partial A} = \frac{1}{A} \tag{A5}$$

$$\frac{\partial \ln p}{\partial \lambda_c} = \begin{cases} \frac{\gamma_1}{\lambda_c}, & \lambda < \lambda_c \\ \frac{\gamma_2}{\lambda_c}, & \lambda > \lambda_c \end{cases}, \tag{A6}$$

$$\frac{\partial \ln p}{\partial \gamma_1} = \begin{cases} -\ln\left(\frac{\lambda}{\lambda_c}\right), & \lambda < \lambda_c \\ 0, & \lambda > \lambda_c \end{cases}, \tag{A7}$$

$$\frac{\partial \ln p}{\partial \gamma_2} = \begin{cases} 0, \ \lambda < \lambda_c, \\ -\ln\left(\frac{\lambda}{\lambda_c}\right), \ \lambda > \lambda_c \end{cases}. \tag{A8}$$

$\nabla \ln \mathcal{L}$ corresponding to Equation (16) can then be expressed as follows:

$$\begin{aligned} \frac{\partial \ln \mathcal{L}}{\partial A_{ij}} &= -n_{ij}^{\rm gal}\left[\frac{\partial I}{\partial A}(\gamma_{1,ij}, \lambda_{\rm min}, \lambda_{c,ij}, A_{ij}, \lambda_{c,ij}; M_{\star,i}, z_j)\right. \\ &\left. + \frac{\partial I}{\partial A}(\gamma_{2,ij}, \lambda_{c,ij}, +\infty, A_{ij}, \lambda_{c,ij}; M_{\star,i}, z_j)\right] \\ &+ \sum_{s=1}^{n_{ij}^{\rm AGN}} \frac{\partial \ln p}{\partial A}(\lambda_s; A_{ij}, \lambda_{c,ij}, \gamma_{1,ij}, \gamma_{2,ij}) \end{aligned} \tag{A9}$$

$$\begin{aligned} \frac{\partial \ln \mathcal{L}}{\partial \lambda_{c,ij}} &= -n_{ij}^{\rm gal}\left[\frac{\partial I}{\partial \lambda_2}(\gamma_{1,ij}, \lambda_{\rm min}, \lambda_{c,ij}, A_{ij}, \lambda_{c,ij}; M_{\star,i}, z_j)\right. \\ &+ \frac{\partial I}{\partial \lambda_c}(\gamma_{1,ij}, \lambda_{\rm min}, \lambda_{c,ij}, A_{ij}, \lambda_{c,ij}; M_{\star,i}, z_j) \\ &+ \frac{\partial I}{\partial \lambda_1}(\gamma_{2,ij}, \lambda_{c,ij}, +\infty, A_{ij}, \lambda_{c,ij}; M_{\star,i}, z_j) \\ &\left. + \frac{\partial I}{\partial \lambda_c}(\gamma_{2,ij}, \lambda_{c,ij}, +\infty, A_{ij}, \lambda_{c,ij}; M_{\star,i}, z_j)\right] \\ &+ \sum_{s=1}^{n_{ij}^{\rm AGN}} \frac{\partial \ln p}{\partial \lambda_c}(\lambda_s; A_{ij}, \lambda_{c,ij}, \gamma_{1,ij}, \gamma_{2,ij}), \end{aligned} \tag{A10}$$

$$\begin{aligned} \frac{\partial \ln \mathcal{L}}{\partial \gamma_{k,ij}} &= -n_{ij}^{\rm gal}\frac{\partial I}{\partial \gamma}(\gamma_{k,ij}, \lambda_{\rm min}, \lambda_{c,ij}, A_{ij}, \lambda_{c,ij}; M_{\star,i}, z_j) \\ &+ \sum_{s=1}^{n_{ij}^{\rm AGN}} \frac{\partial \ln p}{\partial \gamma_k}(\lambda_s; A_{ij}, \lambda_{c,ij}, \gamma_{1,ij}, \gamma_{2,ij}) \\ &(k = 1, 2). \end{aligned} \tag{A11}$$

The partial derivatives of $\ln \pi_{\rm cont}$ in Equation (19) are

$$\begin{aligned} \frac{\partial \ln \pi_{\rm cont}}{\partial X_{ij}} &= \frac{N_M(X_{i-1,j} + X_{i+1,j} - 2X_{ij})}{\sigma_X^2} \\ &+ \frac{N_z(X_{i,j-1} + X_{i,j+1} - 2X_{ij})}{\sigma_X^2}, \end{aligned} \tag{A12}$$

in which X denotes each one of ($\log A$, $\log \lambda_c$, γ_1, γ_2), and we define $X_{0j} \equiv X_{1j}$, $X_{N_M+1,j} \equiv X_{N_M,j}$, $X_{i0} \equiv X_{i1}$, and $X_{i,N_z+1} \equiv X_{i,N_z}$ to incorporate X's at the boundary.

The gradient of the log-posterior in Equation (20) is thus

$$\nabla \ln \mathcal{P} = \sum_{\rm field} \nabla \ln \mathcal{L} + \nabla \ln \pi_{\rm cont}. \tag{A13}$$

When transforming the parameter space, the gradient of the corresponding Jacobian should also be added.

Appendix B
Gradient of the Posterior with the SMF-XLF Constraints Added

This appendix presents the gradient of our posterior after adding the SMF-XLF constraints in Equation (29). First, the partial derivatives of $\psi(\gamma, M_1, M_2, A, \lambda_c; L_{\rm X})$ in Equation (24) are

$$\frac{\partial \psi}{\partial A} = \frac{\psi}{A}, \tag{B1}$$

$$\frac{\partial \psi}{\partial \lambda_c} = \frac{\gamma \psi}{\lambda_c}, \tag{B2}$$

$$\begin{aligned} \frac{\partial \psi}{\partial \gamma} &= A\left(\frac{L_{\rm X}}{M_c \lambda_c}\right)^{-\gamma}\phi_1\left[\frac{\partial \Gamma_{\rm GI}}{\partial \zeta}\left(\alpha_1 + \gamma + 1, \frac{M_1}{M_c}, \frac{M_2}{M_c}\right)\right. \\ &\left. - \ln\left(\frac{L_{\rm X}}{M_c \lambda_c}\right)\Gamma_{\rm GI}\left(\alpha_1 + \gamma + 1, \frac{M_1}{M_c}, \frac{M_2}{M_c}\right)\right] \\ &+ A\left(\frac{L_{\rm X}}{M_c \lambda_c}\right)^{-\gamma}\phi_2\left[\frac{\partial \Gamma_{\rm GI}}{\partial \zeta}\left(\alpha_2 + \gamma + 1, \frac{M_1}{M_c}, \frac{M_2}{M_c}\right)\right. \\ &\left. - \ln\left(\frac{L_{\rm X}}{M_c \lambda_c}\right)\Gamma_{\rm GI}\left(\alpha_2 + \gamma + 1, \frac{M_1}{M_c}, \frac{M_2}{M_c}\right)\right], \end{aligned} \tag{B3}$$

$$\begin{aligned} \frac{\partial \psi}{\partial M_k} &= (2k - 3)\frac{A}{M_c}\left(\frac{L_{\rm X}}{M_c \lambda_c}\right)^{-\gamma} e^{-\frac{M_k}{M_c}} \\ &\times \left[\phi_1\left(\frac{M_k}{M_c}\right)^{\alpha_1+\gamma} + \phi_2\left(\frac{M_k}{M_c}\right)^{\alpha_2+\gamma}\right] \ (k = 1, 2), \end{aligned} \tag{B4}$$

where $\frac{\partial \Gamma_{\rm GI}}{\partial \zeta}(\zeta, x_1, x_2)$ is the partial derivative relative to the first argument of $\Gamma_{\rm GI}(\zeta, x_1, x_2)$. The partial derivatives of $\psi_{\rm DP}(A, \lambda_c, \gamma_1, \gamma_2, M_1, M_2; L_{\rm X})$ in Equation (25) are

$$\frac{\partial \psi_{\rm DP}}{\partial A} = \frac{\psi_{\rm DP}}{A}, \tag{B5}$$

$$\frac{\partial \psi_{\rm DP}}{\partial \lambda_c} = \begin{cases} \frac{\partial \psi}{\partial \lambda_c}(\gamma_2, M_1, M_2, A, \lambda_c), \ \lambda_c < \frac{L_{\rm X}}{M_2} \\ \frac{\partial \psi}{\partial \lambda_c}(\gamma_2, M_1, \frac{L_{\rm X}}{\lambda_c}, A, \lambda_c) \\ + \frac{\partial \psi}{\partial \lambda_c}(\gamma_1, \frac{L_{\rm X}}{\lambda_c}, M_2, A, \lambda_c) \\ - \frac{L_{\rm X}}{\lambda_c^2}\left[\frac{\partial \psi}{\partial M_2}(\gamma_2, M_1, \frac{L_{\rm X}}{\lambda_c}, A, \lambda_c)\right. \\ \left. + \frac{\partial \psi}{\partial M_1}(\gamma_1, \frac{L_{\rm X}}{\lambda_c}, M_2, A, \lambda_c)\right], \frac{L_{\rm X}}{M_2} < \lambda_c < \frac{L_{\rm X}}{M_1} \\ \frac{\partial \psi}{\partial \lambda_c}(\gamma_1, M_1, M_2, A, \lambda_c), \ \lambda_c > \frac{L_{\rm X}}{M_1} \end{cases}, \tag{B6}$$

$$\frac{\partial \psi_{\rm DP}}{\partial \gamma_1} = \begin{cases} 0, \ \lambda_c < \frac{L_{\rm X}}{M_2} \\ \frac{\partial \psi}{\partial \gamma}(\gamma_1, \frac{L_{\rm X}}{\lambda_c}, M_2, A, \lambda_c), \ \frac{L_{\rm X}}{M_2} < \lambda_c < \frac{L_{\rm X}}{M_1} \\ \frac{\partial \psi}{\partial \gamma}(\gamma_1, M_1, M_2, A, \lambda_c), \ \lambda_c > \frac{L_{\rm X}}{M_1} \end{cases}, \tag{B7}$$

$$\frac{\partial \psi_{\rm DP}}{\partial \gamma_2} = \begin{cases} \dfrac{\partial \psi}{\partial \gamma}(\gamma_2, M_1, M_2, A, \lambda_c), \lambda_c < \dfrac{L_{\rm X}}{M_2} \\ \dfrac{\partial \psi}{\partial \gamma}(\gamma_2, M_1, \dfrac{L_{\rm X}}{\lambda_c}, A, \lambda_c), \dfrac{L_{\rm X}}{M_2} < \lambda_c < \dfrac{L_{\rm X}}{M_1} \\ 0, \lambda_c > \dfrac{L_{\rm X}}{M_1} \end{cases}. \quad \text{(B8)}$$

Based on Equation (26), we have

$$\frac{\partial \phi_{L,\rm mdl}}{\partial X_{ij}}(L_{\rm X}, z) = \delta_{jj_z} \times \frac{\partial \psi_{\rm DP}}{\partial X}(A_{ij_z}, \lambda_{c,ij_z}, \gamma_{1,ij_z}, \gamma_{2,ij_z}, M_{LB,i}, M_{LB,i+1}; L_{\rm X}), \quad \text{(B9)}$$

where $\delta_{jj_z} = 0\,(1)$ if $j \neq j_z\,(j = j_z)$, and X denotes each one of $(A,\ \lambda_c,\ \gamma_1,\ \gamma_2)$. The partial derivatives of $\ln \mathcal{L}_{\rm SMF-XLF}$ in Equation (27) are

$$\frac{\partial \ln \mathcal{L}_{\rm SMF-XLF}}{\partial X_{ij}} = \sum_k n_k^{\rm XLF} \left(\frac{1}{\phi_{L,\rm mdl,k}} - \frac{1}{\phi_{L,\rm obs,k}} \right) \frac{\partial \phi_{L,\rm mdl}}{\partial X_{ij}}(L_{{\rm X},k}, z_k). \quad \text{(B10)}$$

The gradient of the posterior in Equation (29) is

$$\nabla \ln \mathcal{P} = \sum_{\rm field} \nabla \ln \mathcal{L} + \nabla \ln \mathcal{L}_{\rm SMF-XLF} + \nabla \ln \pi_{\rm cont}, \quad \text{(B11)}$$

where $\nabla \ln \mathcal{L}$ and $\nabla \ln \pi_{\rm cont}$ were presented in Appendix A.

Appendix C
Results without eFEDS

eFEDS is primarily observed through soft X-rays below 2 keV, which are more prone to obscuration compared to our

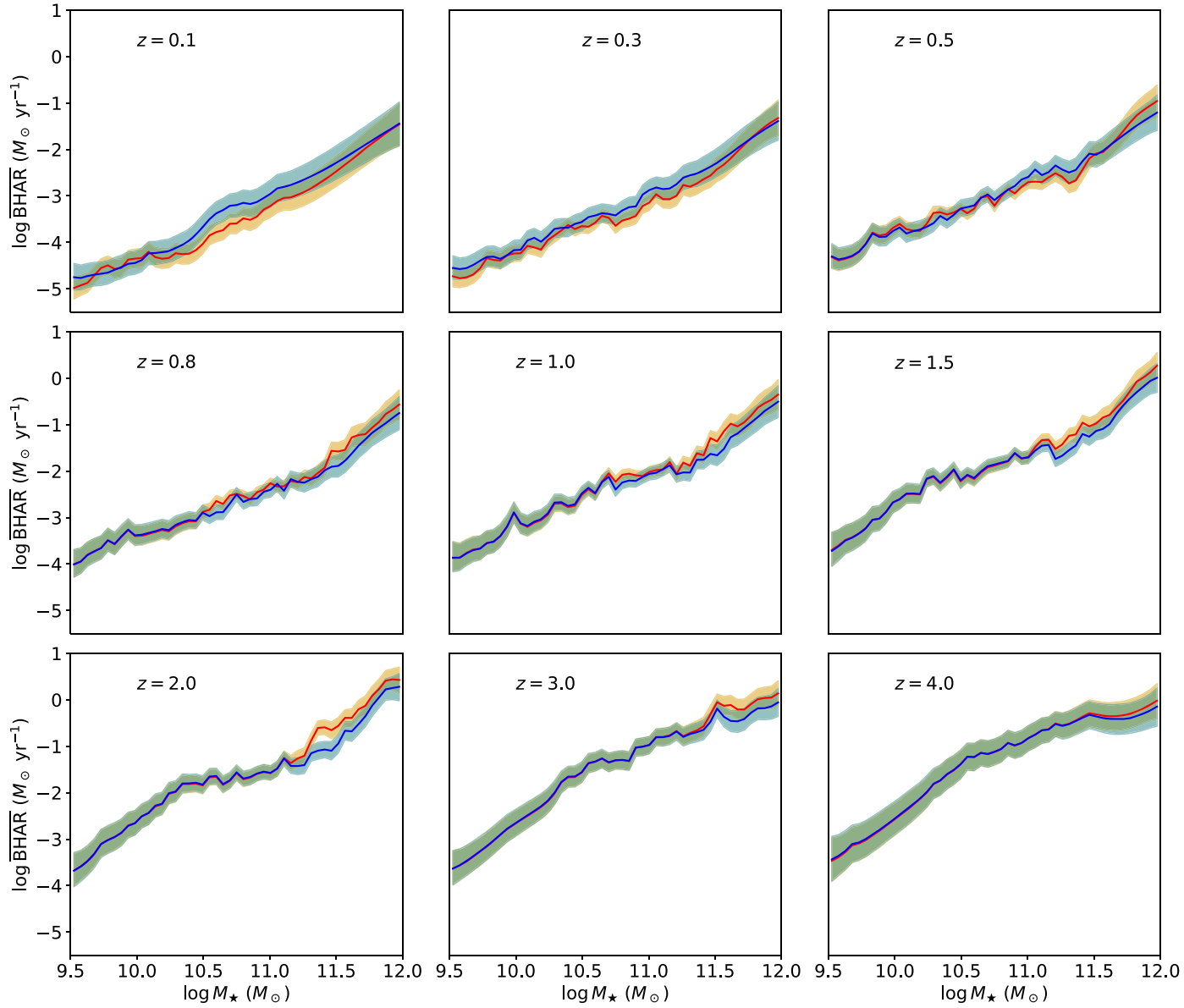

Figure 11. Comparison between $\overline{\rm BHAR}$ with eFEDS included (red) and excluded (blue) in the fitting. The shaded regions represent 1σ uncertainty ranges. The red curves are similar to the blue ones, and the red uncertainties are smaller than the blue ones in certain regimes, indicating that eFEDS does not cause systematic biases and helps constrain $\overline{\rm BHAR}$.

other fields. To examine if our results are biased by this effect, we try excluding eFEDS in this appendix, and the corresponding $\overline{\mathrm{BHAR}}$ results are shown in Figure 11. There is not any material systematic difference in the median $\overline{\mathrm{BHAR}}$ after excluding eFEDS, and the uncertainty becomes larger in certain parameter ranges; e.g., the difference in width of the shaded regions in Figure 11 is apparent at $M_\star \approx 10^{10.8}\,M_\odot$ and $z = 0.5$. The uncertainties generally grow by no more than 60%. Therefore, no strong systematic biases are introduced by eFEDS, and eFEDS also helps constrain $\overline{\mathrm{BHAR}}$. This verifies that the absorption effects have been appropriately considered, as detailed in Section 3.1.1. Besides, given that the LSST DDFs already cover $12.6\,\mathrm{deg}^2$ with sensitive HB data, eFEDS provides useful constraints but is not fully dominant.

Appendix D
Impact of AGN-dominated Sources

It is generally more challenging to reliably measure $M_\star$ from the galaxy component for sources with SEDs dominated by the AGN component. We assess whether the less reliable $M_\star$ measurements for such sources have a strong impact on our $\overline{\mathrm{BHAR}}$ results. It has been shown that the CANDELS fields are largely free from this potential issue (Aird et al. 2018; Yang et al. 2018) due to their small solid angles, superb multi-wavelength coverage, and deep X-ray surveys. For the LSST DDFs and eFEDS, their X-ray surveys are wider and shallower, and thus a larger fraction of the detected AGNs are luminous and may dominate the SEDs. We thus primarily focus on the AGN-dominated sources in the LSST DDFs and eFEDS.

$M_\star$ is largely constrained by the rest-frame near-infrared (NIR) data because the old-star emission peaks in the NIR. For the purpose of assessing the $M_\star$ measurements, we define a source to be *AGN dominated* if its AGN component contributes >50% of the rest-frame 1 μm light, as measured from its decomposed SED. A similar definition was also adopted in Aird et al. (2018). About 10%–15% of our AGNs are classified as AGN dominated. Note that this definition significantly overlaps but is not the same as the broad-line AGN definition. In a general sense, broad-line AGNs are sources with strong AGN signatures (e.g., spectroscopically detected broad emission lines) in the optical. However, a large fraction of broad-line AGNs are not necessarily AGN dominated in the NIR because the galaxy emission usually reaches a peak, while the AGN emission reaches a valley in the NIR. We found that around half of the broad-line AGNs in Ni et al. (2021a) are classified as AGN dominated under our definition, and the non-AGN-dominated ones indeed generally have lower L_X. We adopt our current definition because it is simpler and also more physically related to the $M_\star$ measurement.

We remove AGN-dominated sources in the LSST DDFs and eFEDS and measure $\overline{\mathrm{BHAR}}$ again following Section 3.3. We further estimate the AGN number density maps in the ($M_\star$, z) plane using kernel density estimations before and after excluding these AGN-dominated sources and apply the number density ratio as a function of ($M_\star$, z) as a correction of $\overline{\mathrm{BHAR}}$ to account for the fact that fewer AGNs are included after removing AGN-dominated sources. These procedures are conducted for the whole population as well as star-forming and quiescent galaxies. We compare $\overline{\mathrm{BHAR}}$ with the original ones in Figure 12. The quiescent curves almost do not change after removing AGN-dominated sources, while the whole population and star-forming $\overline{\mathrm{BHAR}}$ become slightly smaller. The difference at high redshift is slightly larger than that at low redshift because high-z sources need higher L_X to be detected in the X-ray and are hence more likely to be AGN-dominated, but the difference is still generally no more than the 1σ uncertainties. Besides, our number-based correction underestimates the real loss of accretion power because AGN-dominated sources, by construction, tend to have higher λ than the remaining ones. The difference in $\overline{\mathrm{BHAR}}$ should be even smaller. Therefore, the relatively larger $M_\star$ uncertainties of AGN-dominated sources are not expected to cause material biases to our $\overline{\mathrm{BHAR}}$.

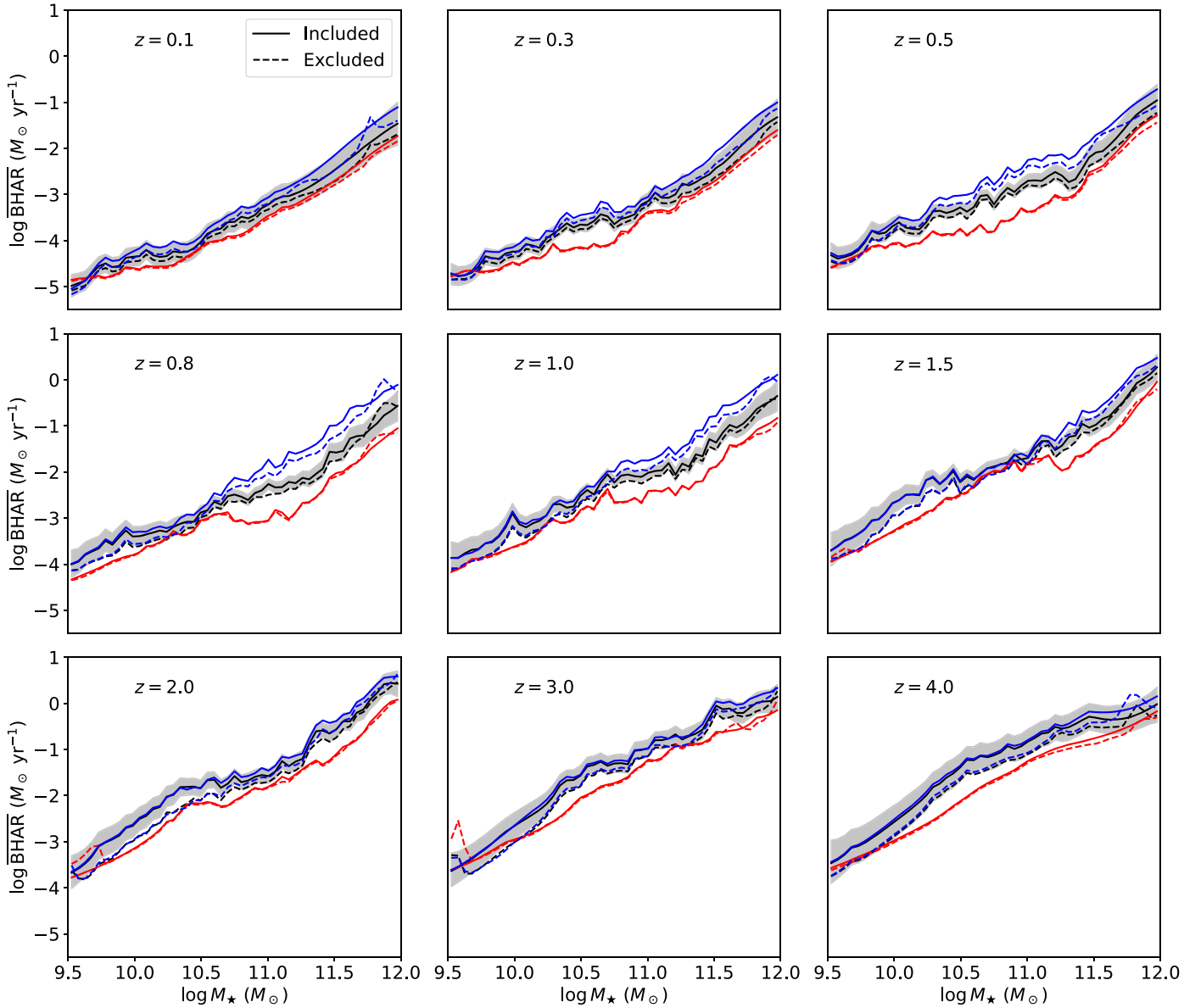

Figure 12. Comparison between $\overline{\mathrm{BHAR}}$ with AGN-dominated sources included (solid curves) and excluded (dashed curves) in the fitting. Black, blue, and red curves represent the whole population, star-forming galaxies, and quiescent galaxies, respectively. The gray-shaded regions denote the 1σ uncertainty ranges of the black solid curves. The solid and dashed $\overline{\mathrm{BHAR}}$ curves are generally consistent within 1σ uncertainties, indicating that AGN-dominated sources do not cause material biases in our results.

ORCID iDs

Fan Zou https://orcid.org/0000-0002-4436-6923
Zhibo Yu https://orcid.org/0000-0002-6990-9058
W. N. Brandt https://orcid.org/0000-0002-0167-2453
Hyungsuk Tak https://orcid.org/0000-0003-0334-8742
Guang Yang https://orcid.org/0000-0001-8835-7722
Qingling Ni https://orcid.org/0000-0002-8577-2717

References

Aird, J., Coil, A. L., & Georgakakis, A. 2017, MNRAS, 465, 3390
Aird, J., Coil, A. L., & Georgakakis, A. 2018, MNRAS, 474, 1225
Aird, J., Coil, A. L., & Georgakakis, A. 2019, MNRAS, 484, 4360
Aird, J., Coil, A. L., & Kocevski, D. D. 2022, MNRAS, 515, 4860
Aird, J., Coil, A. L., Moustakas, J., et al. 2012, ApJ, 746, 90
Ananna, T. T., Treister, E., Urry, C. M., et al. 2019, ApJ, 871, 240
Barro, G., Pérez-González, P. G., Cava, A., et al. 2019, ApJS, 243, 22
Bayer, A. E., Seljak, U., & Modi, C. 2023, arXiv:2307.09504
Betancourt, M. 2017, arXiv:1701.02434
Birchall, K. L., Watson, M. G., & Aird, J. 2020, MNRAS, 492, 2268
Birchall, K. L., Watson, M. G., Aird, J., & Starling, R. L. C. 2023, MNRAS, 523, 4756
Bongiorno, A., Merloni, A., Brusa, M., et al. 2012, MNRAS, 427, 3103
Bongiorno, A., Schulze, A., Merloni, A., et al. 2016, A&A, 588, A78
Brandt, W. N., & Alexander, D. M. 2015, A&ARv, 23, 1
Brandt, W. N., Ni, Q., Yang, G., et al. 2018, arXiv:1811.06542
Brandt, W. N., & Yang, G. 2022, in Handbook of X-Ray and Gamma-Ray Astrophysics, ed. C. Bambi & A. Santangelo (New York: Springer), 78
Brunner, H., Liu, T., Lamer, G., et al. 2022, A&A, 661, A1
Chen, C. T. J., Brandt, W. N., Luo, B., et al. 2018, MNRAS, 478, 2132
Civano, F., Marchesi, S., Comastri, A., et al. 2016, ApJ, 819, 62
Cristello, N., Zou, F., Brandt, W. N., et al. 2024, ApJ, 962, 156
Donnari, M., Pillepich, A., Nelson, D., et al. 2019, MNRAS, 485, 4817
Driver, S. P., Bellstedt, S., Robotham, A. S. G., et al. 2022, MNRAS, 513, 439
Duras, F., Bongiorno, A., Ricci, F., et al. 2020, A&A, 636, A73
Feldmann, R. 2017, MNRAS, 470, L59
Gehrels, N. 1986, ApJ, 303, 336
Georgakakis, A., Aird, J., Schulze, A., et al. 2017, MNRAS, 471, 1976

Georgakakis, A., Nandra, K., Laird, E. S., Aird, J., & Trichas, M. 2008, MNRAS, 388, 1205
Grogin, N. A., Kocevski, D. D., Faber, S. M., et al. 2011, ApJS, 197, 35
Habouzit, M., Somerville, R. S., Li, Y., et al. 2022, MNRAS, 509, 3015
Hickox, R. C., Mullaney, J. R., Alexander, D. M., et al. 2014, ApJ, 782, 9
Jarvis, M. J., Bonfield, D. G., Bruce, V. A., et al. 2013, MNRAS, 428, 1281
Kocevski, D. D., Hasinger, G., Brightman, M., et al. 2018, ApJS, 236, 48
Koekemoer, A. M., Faber, S. M., Ferguson, H. C., et al. 2011, ApJS, 197, 36
Kormendy, J., & Ho, L. C. 2013, ARA&A, 51, 511
Laigle, C., McCracken, H. J., Ilbert, O., et al. 2016, ApJS, 224, 24
Leja, J., Carnall, A. C., Johnson, B. D., Conroy, C., & Speagle, J. S. 2019, ApJ, 876, 3
Liu, T., Buchner, J., Nandra, K., et al. 2022, A&A, 661, A5
Loredo, T. J. 2004, in AIP Conf. Proc. 735, Bayesian Inference and Maximum Entropy Methods in Science and Engineering, ed. R. Fischer, R. Preuss, & U. V. Toussaint (Melville, NY: AIP), 195
Luo, B., Brandt, W. N., Xue, Y. Q., et al. 2017, ApJS, 228, 2
Lusso, E., Comastri, A., Simmons, B. D., et al. 2012, MNRAS, 425, 623
Marchesi, S., Civano, F., Elvis, M., et al. 2016, ApJ, 817, 34
Nandra, K., Laird, E. S., Aird, J. A., et al. 2015, ApJS, 220, 10
Ni, Q., Brandt, W. N., Chen, C.-T., et al. 2021a, ApJS, 256, 21
Ni, Q., Brandt, W. N., Yang, G., et al. 2021b, MNRAS, 500, 4989
Ni, Q., Yang, G., Brandt, W. N., et al. 2019, MNRAS, 490, 1135
Popesso, P., Concas, A., Cresci, G., et al. 2023, MNRAS, 519, 1526
Pozzetti, L., Bolzonella, M., Zucca, E., et al. 2010, A&A, 523, A13
Rasmussen, C. E., & Williams, C. K. I. 2006, Gaussian Processes for Machine Learning (Cambridge, MA: MIT Press)
Ricci, C., Trakhtenbrot, B., Koss, M. J., et al. 2017, Natur, 549, 488
Salvato, M., Wolf, J., Dwelly, T., et al. 2022, A&A, 661, A3
Santini, P., Ferguson, H. C., Fontana, A., et al. 2015, ApJ, 801, 97
Stefanon, M., Yan, H., Mobasher, B., et al. 2017, ApJS, 229, 32
Tak, H., Ghosh, S. K., & Ellis, J. A. 2018, MNRAS, 481, 277
Ueda, Y., Akiyama, M., Hasinger, G., Miyaji, T., & Watson, M. G. 2014, ApJ, 786, 104
Wang, T., Elbaz, D., Alexander, D. M., et al. 2017, A&A, 601, A63
Weaver, J. R., Kauffmann, O. B., Ilbert, O., et al. 2022, ApJS, 258, 11
Wright, A. H., Driver, S. P., & Robotham, A. S. G. 2018, MNRAS, 480, 3491
Xue, Y. Q., Luo, B., Brandt, W. N., et al. 2016, ApJS, 224, 15
Yan, W., Brandt, W. N., Zou, F., et al. 2023, ApJ, 951, 27
Yang, G., Brandt, W. N., Alexander, D. M., et al. 2019, MNRAS, 485, 3721
Yang, G., Brandt, W. N., Luo, B., et al. 2016, ApJ, 831, 145
Yang, G., Brandt, W. N., Vito, F., et al. 2018, MNRAS, 475, 1887
Yang, G., Caputi, K. I., Papovich, C., et al. 2023, ApJL, 950, L5
Yang, G., Chen, C. T. J., Vito, F., et al. 2017, ApJ, 842, 72
Yang, G., Estrada-Carpenter, V., Papovich, C., et al. 2021, ApJ, 921, 170
Yu, Z., Zou, F., & Brandt, W. N. 2023, RNAAS, 7, 248
Yuan, F., & Narayan, R. 2014, ARA&A, 52, 529
Zou, F., Brandt, W. N., Chen, C.-T., et al. 2022, ApJS, 262, 15
Zou, F., Brandt, W. N., Ni, Q., et al. 2023, ApJ, 950, 136
Zou, F., Yang, G., Brandt, W. N., et al. 2021, RNAAS, 5, 56